

## Fast parallel IGA-ADS solver for time-dependent Maxwell's equations

Marcin Łoś<sup>a</sup>, Maciej Woźniak<sup>a</sup>, Keshav Pingali<sup>c</sup>, Luis Emilio Garcia Castillo<sup>b</sup>,  
Julen Alvarez-Aramberri<sup>d</sup>, David Pardo<sup>d,e,f</sup>, Maciej Paszyński<sup>a,\*</sup>

<sup>a</sup> AGH University of Kraków, Poland

<sup>b</sup> University of Carlos III Madrid, Spain

<sup>c</sup> Oden Institute, The University of Texas at Austin, USA

<sup>d</sup> University of the Basque Country (UPV/EHU), Leioa, Spain

<sup>e</sup> Basque Center for Applied Mathematics (BCAM), Bilbao, Spain

<sup>f</sup> Ikerbasque, Bilbao, Spain

### ARTICLE INFO

#### Keywords:

Variational splitting

Time-dependent Maxwell

Absorbing boundary conditions

Isogeometric analysis

### ABSTRACT

We propose a simulator for time-dependent Maxwell's equations with linear computational cost. We employ B-spline basis functions as considered in the isogeometric analysis (IGA). We focus on non-stationary Maxwell's equations defined on a regular patch of elements. We employ the idea of alternating-directions splitting (ADS) and employ a second-order accurate time-integration scheme for the time-dependent Maxwell's equations in a weak form. After discretization, the resulting stiffness matrix exhibits a Kronecker product structure. Thus, it enables linear computational cost LU factorization. Additionally, we derive a formulation for absorbing boundary conditions (ABCs) suitable for direction splitting. We perform numerical simulations of the scattering problem (traveling pulse wave) to verify the ABC. We simulate the radiation of electromagnetic (EM) waves from the dipole antenna. We verify the order of the time integration scheme using a manufactured solution problem. We then simulate magnetotelluric measurements. Our simulator is implemented in a shared memory parallel machine, with the GALOIS library supporting the parallelization. We illustrate the parallel efficiency with strong and weak scalability tests corresponding to non-stationary Maxwell simulations.

### 1. Introduction

There are two main approaches for solving Maxwell's Equations, i.e., working in the so-called frequency domain or in the time domain, having both advantages and limitations depending on the particular problem to solve. Working in the frequency domain is very popular in the field of electrical & telecommunication engineering and implies the use of the Fourier transform version of Maxwell's Equations, i.e., the time-harmonic case. That has the advantage that each simulation (at a given frequency) can be carried out independently. It also allows us to naturally take into account variations of the material properties (material constants) with frequency. On the other hand, the characterization of the problem at hand withing a given (possibly wide) frequency band or the capture of some transient responses (using inverse Fourier transform) requires of quite a number of simulations at different frequencies. Despite the fact that there are “fast frequency sweeps” methods for that and that simulations for the time harmonic case are relatively cheap (compared to the general time-dependent simulations),

it may be that they are not competitive. On the other hand, time-dependent formulations naturally deliver transient responses and are able to easily take into account changes of material constants at different time steps; being appropriate to model non-linear problems. They provide, by using the inverse Fourier transform, the frequency characterization of a problem on single run. On the contrary, time-dependent simulations involves high computational time and may suffer from instabilities.

In this paper, we propose a time-dependent simulator employing an implicit time integration scheme preserving the Kronecker product structure of matrices, and thus resulting in a linear computational cost. One challenging aspect of such an approach is the imposition of boundary conditions. When dealing with open region wave propagation problems, the original mathematical domain of the problem is infinite. Thus, in order to analyze it using computers the infinite domain must be truncated. A suitable boundary condition needs to be used on that boundary. One commonly considered type of boundary condition for the truncation boundary with electromagnetic simulations is the so

\* Corresponding author.

E-mail address: [los@agh.edu.pl](mailto:los@agh.edu.pl) (M. Łoś).

<https://doi.org/10.1016/j.camwa.2023.09.035>

called Absorbing Boundary Conditions (ABCs), which allow the waves to freely propagate through the boundary without generating artificial reflected waves back into the domain. Numerous numerical methods for this type of boundary conditions have been developed over the years [2,3]. Since these boundary conditions are essentially non-local (in both space and time), practical calculations employ some approximations [2]. While some exact methods have been proposed [1,4–6], these methods are not suitable for direction splitting, and implementing them will require a computational cost higher than  $\mathcal{O}(N)$  per timestep, where  $N$  is the number of degrees of freedom. In our paper we propose an implementation of ABC suitable for direction splitting solver, with computational cost  $\mathcal{O}(N)$ .

We propose a linear computational cost isogeometric finite element method solver for time-dependent Maxwell’s equations in three dimensions. Our solver employs the variational splitting method, introduced in [7], and the second-order implicit time integration scheme proposed in [8,9]. We discretize with high-order B-splines from the isogeometric finite element method (IGA-FEM) [10]. The application of the variational splitting method for the implicit time integration scheme delivers the Kronecker product structure of the matrix and the linear computational cost of the solver. Thus, we propose a fast IGA-FEM solver for 3D non-stationary Maxwell’s equations. Our method is implemented in open-source IGA-ADS software [11]. It uses the GALOIS environment for shared-memory parallelization [12,13].

The application of a variational splitting method in isogeometric analysis originated in the works of Gao and Calo [14,15]. They proposed the decomposition of the mass matrix with tensor product B-spline basis functions into the Kronecker product of several one-dimensional mass matrices. It has been later applied to explicit dynamics simulations [16,17], with the mass matrix on the left-hand side and fast parallel integration of the right-hand sides with GALOIS environment [12,13]. The variational splitting has also been employed within higher-order implicit time integration schemes [7,18,19], using the approximation of the linear combination of the mass and stiffness matrices by a Kronecker product of one-dimensional matrices. The variational splitting can also be integrated with alternating directions techniques introduced in the context of finite difference simulations [20,21].

Our non-stationary Maxwell solver is augmented with Dirichlet, Neumann, or Absorbing Boundary Conditions (ABCs). In particular, we derive an ABC formulation that preserves our simulator’s linear computational cost. The ABC is often formulated in the frequency domain [23], while in this work we derive it in the non-stationary setup. We verify our non-stationary solver and the second order time integration scheme using a manufactured solution technique. For that, we consider a traveling pulse wave model. We also simulate the radiation phenomenon from the dipole antenna, and we compare it against the known exact solution. Additionally, we perform simulations of magnetotelluric measurements.

The structure of the paper is the following. We start from derivation in Section 2 of the implicit time integration scheme allowing direction splitting. We continue with the B-spline discretization in Section 3 and the Kronecker product structure of the derived matrices. Section 4 is devoted to the derivation of the Absorbing Boundary Conditions suitable for direction splitting. We summarize our formulations in Section 5. Numerical results presented in Section 6 concern the traveling pulse wave, the radiation from the dipole antenna with a known exact solution, the manufactured solution problem used to verify the order of the time integration scheme, and the magnetotelluric simulations used for identification of the conductivity of the formation layers. In Section 7, we discuss the parallel scalability of the code. Finally, we summarize the work in Section 8.

## 2. Variational splitting for time-dependent Maxwell’s equations

We start from the time-dependent Maxwell’s equations

$$\begin{aligned} \partial_t \mathbf{E} &= \frac{1}{\epsilon} \nabla \times \mathbf{H}, \\ \partial_t \mathbf{H} &= -\frac{1}{\mu} \nabla \times \mathbf{E} \end{aligned} \tag{1}$$

that model electrodynamics on some source-free spatial domain  $\Omega$  and time interval  $[0, T]$ , where  $\mathbf{E}$  denotes the electric field,  $\mathbf{H}$  stands for the magnetic field,  $\epsilon$  is the permittivity, and  $\mu$  is the permeability. We perform the following splitting for the rotational operator

$$\nabla \times = \begin{bmatrix} 0 & -\partial_3 & \partial_2 \\ \partial_3 & 0 & -\partial_1 \\ -\partial_2 & \partial_1 & 0 \end{bmatrix} = \underbrace{\begin{bmatrix} 0 & 0 & \partial_2 \\ \partial_3 & 0 & 0 \\ 0 & \partial_1 & 0 \end{bmatrix}}_{C_1} - \underbrace{\begin{bmatrix} 0 & \partial_3 & 0 \\ 0 & 0 & \partial_1 \\ \partial_2 & 0 & 0 \end{bmatrix}}_{C_2}. \tag{2}$$

The splitting verifies:

$$C_1 C_2 = \begin{bmatrix} \partial_2^2 & 0 & 0 \\ 0 & \partial_3^2 & 0 \\ 0 & 0 & \partial_1^2 \end{bmatrix}, \quad C_2 C_1 = \begin{bmatrix} \partial_3^2 & 0 & 0 \\ 0 & \partial_1^2 & 0 \\ 0 & 0 & \partial_2^2 \end{bmatrix}, \tag{3}$$

which allows keeping the equations for each field components independent. Other properties are the following

$$C_1 C_1 = \begin{bmatrix} 0 & \partial_2 \partial_1 & 0 \\ 0 & 0 & \partial_3 \partial_2 \\ \partial_1 \partial_3 & 0 & 0 \end{bmatrix}, \quad C_2 C_2 = \begin{bmatrix} 0 & 0 & \partial_3 \partial_1 \\ \partial_1 \partial_2 & 0 & 0 \\ 0 & \partial_2 \partial_3 & 0 \end{bmatrix}, \tag{4}$$

and these terms in the time integration scheme will be kept on the right-hand side.

Let us discretize the time by dividing  $[0, T]$  into  $N$  subintervals of size  $\tau = T/N$ . We wish to compute approximate values of the electric and magnetic fields  $\mathbf{E}^n \approx \mathbf{E}(t^n)$ ,  $\mathbf{H}^n \approx \mathbf{H}(t^n)$  at time points  $t^n = n\tau$  for  $n = 0, 1, \dots, N$ . The time marching scheme employing the above decomposition is constructed by splitting each time step of the simulation into sub-steps and introducing in-between unknowns  $\mathbf{E}^{n+\frac{1}{2}}$  and  $\mathbf{H}^{n+\frac{1}{2}}$ . Let  $\tau$  denote the size of the full time step. We can approximate the time derivatives on the left-hand side of the Maxwell’s equations at  $t = t^{n+\frac{1}{2}}$  by finite differences

$$\partial_t \mathbf{E} = \frac{\mathbf{E}^{n+\frac{1}{2}} - \mathbf{E}^n}{\tau/2} = \frac{1}{\epsilon} \nabla \times \mathbf{H}; \quad \partial_t \mathbf{H} = \frac{\mathbf{H}^{n+\frac{1}{2}} - \mathbf{H}^n}{\tau/2} = -\frac{1}{\mu} \nabla \times \mathbf{E}, \tag{5}$$

and similarly for  $t = t^{n+1}$ . In each sub-step, we construct the right-hand side by splitting the rotation operator applied to  $\mathbf{E}$  and  $\mathbf{H}$  into its  $C_1$  and  $C_2$  parts, and treating one of these implicitly, and the other explicitly. In more detail, in the first sub-step we compute  $\mathbf{E}^{n+\frac{1}{2}}$  and  $\mathbf{H}^{n+\frac{1}{2}}$  given the previous time step solution  $\mathbf{E}^n$  and  $\mathbf{H}^n$  by solving the system

$$\begin{aligned} \mathbf{E}^{n+\frac{1}{2}} &= \mathbf{E}^n + \frac{\tau}{2\epsilon} \underbrace{\left( C_1 \mathbf{H}^{n+\frac{1}{2}} - C_2 \mathbf{H}^n \right)}_{\nabla \times \mathbf{H}}, \\ \mathbf{H}^{n+\frac{1}{2}} &= \mathbf{H}^n - \frac{\tau}{2\mu} \underbrace{\left( C_1 \mathbf{E}^n - C_2 \mathbf{E}^{n+\frac{1}{2}} \right)}_{\nabla \times \mathbf{E}}, \end{aligned} \tag{6}$$

and in the second sub-step we compute  $\mathbf{E}^{n+1}$  and  $\mathbf{H}^{n+1}$  by solving

$$\begin{aligned} \mathbf{E}^{n+1} &= \mathbf{E}^{n+\frac{1}{2}} + \frac{\tau}{2\epsilon} \underbrace{\left( C_1 \mathbf{H}^{n+\frac{1}{2}} - C_2 \mathbf{H}^{n+1} \right)}_{\nabla \times \mathbf{H}}, \\ \mathbf{H}^{n+1} &= \mathbf{H}^{n+\frac{1}{2}} - \frac{\tau}{2\mu} \underbrace{\left( C_1 \mathbf{E}^{n+1} - C_2 \mathbf{E}^{n+\frac{1}{2}} \right)}_{\nabla \times \mathbf{E}}. \end{aligned} \tag{7}$$

Since the systems corresponding to both sub-steps have a very similar structure, we will elucidate the solution method of the first sub-step

with the understanding that the second is solved analogously. To solve the first sub-step, first we insert the second equation of (6) into the corresponding right-hand side of the first equation

$$\begin{aligned} \mathbf{E}^{n+\frac{1}{2}} &= \mathbf{E}^n + \frac{\tau}{2\epsilon} \left( C_1 \underbrace{\left[ \mathbf{H}^n - \frac{\tau}{2\mu} (C_1 \mathbf{E}^n - C_2 \mathbf{E}^{n+\frac{1}{2}}) \right]}_{\mathbf{H}^{n+\frac{1}{2}}} - C_2 \mathbf{H}^n \right) \\ &= \mathbf{E}^n + \frac{\tau}{2\epsilon} \underbrace{(C_1 \mathbf{H}^n - C_2 \mathbf{H}^n)}_{\nabla \times \mathbf{H}^n} - \frac{\tau^2}{4\epsilon\mu} C_1^2 \mathbf{E}^n + \frac{\tau^2}{4\epsilon\mu} C_1 C_2 \mathbf{E}^{n+\frac{1}{2}}, \end{aligned} \tag{8}$$

to obtain

$$\left( 1 - \frac{\tau^2}{4\epsilon\mu} C_1 C_2 \right) \mathbf{E}^{n+\frac{1}{2}} = \mathbf{E}^n + \frac{\tau}{2\epsilon} \nabla \times \mathbf{H}^n - \underbrace{\frac{\tau^2}{4\epsilon\mu} C_1^2 \mathbf{E}^n}_{\text{inconvenient}}. \tag{9}$$

The matrix on the left-hand side is block-diagonal, and the “inconvenient” off-diagonal terms are on the right-hand side now, so that we can compute each component of  $\mathbf{E}^{n+\frac{1}{2}}$  independently. Once we have  $\mathbf{E}^{n+\frac{1}{2}}$ , unknown  $\mathbf{H}^{n+\frac{1}{2}}$  can be computed directly using the second equation of (6). Let us focus now on the fully expanded first sub-step, introducing  $\lambda = \frac{\tau^2}{4\epsilon\mu}$ .

$$\begin{aligned} (1 - \lambda \partial_2^2) E_1^{n+\frac{1}{2}} &= E_1^n + \frac{\tau}{2\epsilon} (\nabla \times \mathbf{H}^n)_1 - \lambda \partial_2 \partial_1 E_2^n, \\ (1 - \lambda \partial_3^2) E_2^{n+\frac{1}{2}} &= E_2^n + \frac{\tau}{2\epsilon} (\nabla \times \mathbf{H}^n)_2 - \lambda \partial_3 \partial_2 E_3^n, \\ (1 - \lambda \partial_1^2) E_3^{n+\frac{1}{2}} &= E_3^n + \frac{\tau}{2\epsilon} (\nabla \times \mathbf{H}^n)_3 - \lambda \partial_1 \partial_3 E_1^n. \end{aligned} \tag{10}$$

We will derive now the weak formulation for the equations (10) above. We multiply by a test function  $v$ , integrate over  $\Omega$

$$\begin{aligned} &\left( E_1^{n+\frac{1}{2}}, v \right) - \lambda \left( \partial_2^2 E_1^{n+\frac{1}{2}}, v \right) \\ &= (E_1^n, v) + \frac{\tau}{2\epsilon} \left( (\nabla \times \mathbf{H}^n)_1, v \right) - \lambda \left( \partial_2 \partial_1 E_2^n, v \right). \end{aligned} \tag{11}$$

Now, we integrate by parts the terms on the left-hand side to obtain

$$\begin{aligned} \left( E_1^{n+\frac{1}{2}}, v \right) - \lambda \left( \partial_2^2 E_1^{n+\frac{1}{2}}, v \right) &= \left( E_1^{n+\frac{1}{2}}, v \right) + \lambda \left( \partial_2 E_1^{n+\frac{1}{2}}, \partial_2 v \right) \\ &\quad - \lambda \left\langle \partial_2 E_1^{n+\frac{1}{2}}, v n_2 \right\rangle, \end{aligned} \tag{12}$$

$$\begin{aligned} \left( E_2^{n+\frac{1}{2}}, v \right) - \lambda \left( \partial_3^2 E_2^{n+\frac{1}{2}}, v \right) &= \left( E_2^{n+\frac{1}{2}}, v \right) + \lambda \left( \partial_3 E_2^{n+\frac{1}{2}}, \partial_3 v \right) \\ &\quad - \lambda \left\langle \partial_3 E_2^{n+\frac{1}{2}}, v n_3 \right\rangle, \end{aligned} \tag{13}$$

$$\begin{aligned} \left( E_3^{n+\frac{1}{2}}, v \right) - \lambda \left( \partial_1^2 E_3^{n+\frac{1}{2}}, v \right) &= \left( E_3^{n+\frac{1}{2}}, v \right) + \lambda \left( \partial_1 E_3^{n+\frac{1}{2}}, \partial_1 v \right) \\ &\quad - \lambda \left\langle \partial_1 E_3^{n+\frac{1}{2}}, v n_1 \right\rangle. \end{aligned} \tag{14}$$

Here,  $(\cdot, \cdot)$  denotes the scalar product of  $L^2(\Omega)$ ,  $\langle \cdot, \cdot \rangle$  stands for the scalar product of  $L^2(\partial\Omega)$  and  $n$  stands for the unit vector normal to the boundary of  $\Omega$  and pointing outside.

The remaining boundary terms will be used to impose boundary conditions in Section 3. The second sub-step is performed analogously, starting with eq. (7). The roles of  $C_1$  and  $C_2$  in eq. (7) are swapped compared to (6), which leads to  $C_1 C_2$  and  $C_1^2$  in eq. (9) being replaced by  $C_2 C_1$  and  $C_2^2$ , respectively. The final form of the direction splitting scheme depends on the boundary conditions, which will be introduced in Section 3, and the final form of the equations is presented at the end of Section 4.

### 2.1. Regularity of the solutions

Integrating all the terms involving second-order derivatives arising from equation (10) and an analogous equation for  $\mathbf{E}^n$ , we can conclude that for the weak formulation to be well defined we need that:

- $\partial_2 E_1^{n+\frac{1}{2}}, \partial_3 E_2^{n+\frac{1}{2}}, \partial_1 E_3^{n+\frac{1}{2}} \in L^2(\Omega)$
- $\partial_3 E_1^{n+1}, \partial_1 E_2^{n+1}, \partial_2 E_3^{n+1} \in L^2(\Omega)$

Using operators  $C1$  and  $C2$  we can write it concisely as

$$\begin{aligned} \mathbf{E}^{n+\frac{1}{2}} \in H(C_2, \Omega) &:= \{ \mathbf{A} \in L^2(\Omega)^3 : C_2 \mathbf{A} \in L^2(\Omega)^3 \} \\ \mathbf{E}^{n+1} \in H(C_1, \Omega) &:= \{ \mathbf{A} \in L^2(\Omega)^3 : C_1 \mathbf{A} \in L^2(\Omega)^3 \} \end{aligned}$$

These spaces are larger than  $H(\text{curl})$ , but  $H(C_1) \cap H(C_2) \subset H(\text{curl})$ .

Note that we do not explicitly consider the regularity restrictions imposed by the boundary terms, since these will eventually be replaced by the boundary condition data, and thus will not appear in the final formulation.

### 3. Boundary conditions

#### 3.1. First order absorbing boundary conditions (ABCs)

The first order absorbing boundary conditions (ABCs) that we will be using are prescribed as

$$-\hat{\mathbf{n}} \times \mathbf{H} + \frac{1}{\eta} \hat{\mathbf{n}} \times (\hat{\mathbf{n}} \times \mathbf{E}) = \mathbf{E}^{\text{inc}} \tag{15}$$

where  $\eta = \sqrt{\mu/\epsilon}$ , symbol  $\hat{\mathbf{n}}$  denotes the outward unit normal to the considered boundary.

And  $\mathbf{E}^{\text{inc}}$  denotes an incident field (more precisely, the tangential component to the boundary). Boundary condition (15) is the so called radiation condition satisfied exactly at infinite distance from the sources [2,27]. We will use it as boundary condition to truncate the original infinite domain of the problems considered later in the paper. The problem with direct implementation of the ABC in variational splitting solver is that it introduces coupling between  $\mathbf{E}$  and  $\mathbf{H}$ , which in turn interferes with the splitting. Thus, we derive an alternative formulation by computing  $\partial_t(\text{ABC})$ , namely

$$-\hat{\mathbf{n}} \times \underbrace{\partial_t \mathbf{H}}_{-\frac{1}{\mu} \nabla \times \mathbf{E}} + \frac{1}{\eta} \hat{\mathbf{n}} \times (\hat{\mathbf{n}} \times \partial_t \mathbf{E}) = \partial_t \mathbf{E}^{\text{inc}}, \tag{16}$$

which results in Robin type boundary conditions

$$\hat{\mathbf{n}} \times (\nabla \times \mathbf{E}) + \frac{\mu}{\eta} \hat{\mathbf{n}} \times (\hat{\mathbf{n}} \times \partial_t \mathbf{E}) = \mu \partial_t \mathbf{E}^{\text{inc}}. \tag{17}$$

The new boundary condition is obtained by differentiating the original one with respect to the time variable, so the solution with the original BC also satisfies the modified BC. Since the solution is unique, both versions of BC must therefore lead to the same solution, with the same regularity. Since  $\mathbf{a} \times (\mathbf{b} \times \mathbf{c}) = (\mathbf{a} \cdot \mathbf{c}) \mathbf{b} - (\mathbf{a} \cdot \mathbf{b}) \mathbf{c}$  we have

$$\begin{aligned} \hat{\mathbf{n}} \times (\nabla \times \mathbf{E}) &= \nabla (\hat{\mathbf{n}} \cdot \mathbf{E}) - (\hat{\mathbf{n}} \cdot \nabla) \mathbf{E} \\ -\hat{\mathbf{n}} \times (\hat{\mathbf{n}} \times \partial_t \mathbf{E}) &= \partial_t \mathbf{E} - \underbrace{(\hat{\mathbf{n}} \cdot \partial_t \mathbf{E}) \hat{\mathbf{n}}}_{\substack{\text{perpendicular component} \\ \text{of } \partial_t \mathbf{E}}} \\ &\quad \underbrace{\phantom{(\hat{\mathbf{n}} \cdot \partial_t \mathbf{E}) \hat{\mathbf{n}}}}_{\substack{\text{tangential component} \\ \text{of } \partial_t \mathbf{E}}} \end{aligned}$$

For  $\hat{\mathbf{n}} = \pm \hat{\mathbf{e}}_k \in \{(\pm 1, 0, 0), (0, \pm 1, 0), (0, 0, \pm 1)\}$  over the cube we have

$$\hat{\mathbf{n}} \times (\nabla \times \mathbf{E}) = \pm (\nabla E_k - \partial_k \mathbf{E}) = \hat{\mathbf{n}}_k \begin{bmatrix} \partial_1 E_k - \partial_k E_1 \\ \partial_2 E_k - \partial_k E_2 \\ \partial_3 E_k - \partial_k E_3 \end{bmatrix} \tag{18}$$

for  $k = 1, 2, 3$ , meaning  $\partial_k \in \{\partial_1, \partial_2, \partial_3\}$  (which corresponds to spatial directions  $\{\partial_x, \partial_y, \partial_z\}$ ). For the cube-shaped domain, we have  $\hat{n}_k \in \{-1, 1\}$ .

Back to (17), using (18) since for each  $k$  we have only two non-zero components on a cube, and the third one is zero, as well as the perpendicular component is zero in this case

$$-\hat{n} \times (\hat{n} \times \partial_t \mathbf{E}) = \partial_t \mathbf{E} - \underbrace{(\hat{n} \cdot \partial_t \mathbf{E}) \hat{n}}_{\substack{\text{perpendicular component} \\ \text{of } \partial_t \mathbf{E} = 0 \text{ here}}} \underbrace{\phantom{(\hat{n} \cdot \partial_t \mathbf{E}) \hat{n}}}_{\substack{\text{tangential component} \\ \text{of } \partial_t \mathbf{E}}} \tag{19}$$

On the regular cube, this amounts to

- on  $\Gamma_1$ ,  $\hat{n} = \pm \hat{e}_1$ :

$$\hat{n}_1 (\nabla \times \mathbf{E})_3 = -\mu \frac{\partial U_2}{\partial t} - \frac{\mu}{\eta} \partial_t E_2 \tag{20}$$

$$\hat{n}_1 (\nabla \times \mathbf{E})_2 = \mu \frac{\partial U_3}{\partial t} + \frac{\mu}{\eta} \partial_t E_3$$

- on  $\Gamma_2$ ,  $\hat{n} = \pm \hat{e}_2$ :

$$\hat{n}_2 (\nabla \times \mathbf{E})_3 = -\mu \frac{\partial U_1}{\partial t} - \frac{\mu}{\eta} \partial_t E_1 \tag{21}$$

$$\hat{n}_2 (\nabla \times \mathbf{E})_1 = \mu \frac{\partial U_3}{\partial t} + \frac{\mu}{\eta} \partial_t E_3$$

- on  $\Gamma_3$ ,  $\hat{n} = \pm \hat{e}_3$ :

$$\hat{n}_3 (\nabla \times \mathbf{E})_2 = -\mu \frac{\partial U_1}{\partial t} - \frac{\mu}{\eta} \partial_t E_1 \tag{22}$$

$$\hat{n}_3 (\nabla \times \mathbf{E})_1 = \mu \frac{\partial U_2}{\partial t} + \frac{\mu}{\eta} \partial_t E_2$$

The integration by parts in the weak form results in the following boundary terms (and for the simplicity of the presentation, we skip all other terms here):

- On the left-hand side, the strong form term transforms into the following weak form term:

$$-\lambda \partial_2^2 E_1^{n+\frac{1}{2}} \rightarrow -\lambda \left\langle \partial_2 E_1^{n+\frac{1}{2}}, v \hat{n}_2 \right\rangle,$$

$$-\lambda \partial_3^2 E_2^{n+\frac{1}{2}} \rightarrow -\lambda \left\langle \partial_3 E_2^{n+\frac{1}{2}}, v \hat{n}_3 \right\rangle, \tag{23}$$

$$-\lambda \partial_1^2 E_3^{n+\frac{1}{2}} \rightarrow -\lambda \left\langle \partial_1 E_3^{n+\frac{1}{2}}, v \hat{n}_1 \right\rangle.$$

- On the right-hand side, the strong form term transforms into the following weak form term:

$$-\lambda \partial_2 \partial_1 E_2^n \rightarrow -\lambda \left\langle \partial_1 E_2^n, v \hat{n}_2 \right\rangle,$$

$$-\lambda \partial_3 \partial_2 E_3^n \rightarrow -\lambda \left\langle \partial_2 E_3^n, v \hat{n}_3 \right\rangle, \tag{24}$$

$$-\lambda \partial_1 \partial_3 E_1^n \rightarrow -\lambda \left\langle \partial_3 E_1^n, v \hat{n}_1 \right\rangle.$$

In the left-hand side terms, we change  $E^{n+\frac{1}{2}}$  into  $E^n$ , and we move the corresponding terms into the right-hand side. After this modification, each boundary term is non-zero on exactly one of  $\Gamma_1, \Gamma_2, \Gamma_3$ :

$$\lambda \left\langle \partial_2 E_1^n, v n_2 \right\rangle - \lambda \left\langle \partial_1 E_2^n, v n_2 \right\rangle = -\lambda \left\langle \underbrace{-\partial_2 E_1^n + \partial_1 E_2^n}_{(\nabla \times \mathbf{E})_3}, v n_2 \right\rangle,$$

$$\lambda \left\langle \partial_3 E_2^n, v n_3 \right\rangle - \lambda \left\langle \partial_2 E_3^n, v n_3 \right\rangle = -\lambda \left\langle \underbrace{-\partial_3 E_2^n + \partial_2 E_3^n}_{(\nabla \times \mathbf{E})_1}, v n_3 \right\rangle,$$

$$\lambda \left\langle \partial_1 E_3^n, v n_1 \right\rangle - \lambda \left\langle \partial_3 E_1^n, v n_1 \right\rangle = -\lambda \left\langle \underbrace{-\partial_1 E_3^n + \partial_3 E_1^n}_{(\nabla \times \mathbf{E})_2}, v n_1 \right\rangle. \tag{25}$$

Using the boundary conditions, we can rewrite the components of  $\nabla \times \mathbf{E}$  as

$$\left\langle \underbrace{-\partial_2 E_1^n + \partial_1 E_2^n}_{(\nabla \times \mathbf{E})_3}, v n_2 \right\rangle = \left\langle \mu \frac{\partial U_1}{\partial t} + \frac{\mu}{\eta} \partial_t E_1, v \right\rangle_{\Gamma_2},$$

$$\left\langle \underbrace{-\partial_3 E_2^n + \partial_2 E_3^n}_{(\nabla \times \mathbf{E})_1}, v n_3 \right\rangle = \left\langle \mu \frac{\partial U_2}{\partial t} + \frac{\mu}{\eta} \partial_t E_2, v \right\rangle_{\Gamma_3}, \tag{26}$$

$$\left\langle \underbrace{-\partial_1 E_3^n + \partial_3 E_1^n}_{(\nabla \times \mathbf{E})_2}, v n_1 \right\rangle = \left\langle \mu \frac{\partial U_3}{\partial t} + \frac{\mu}{\eta} \partial_t E_3, v \right\rangle_{\Gamma_1},$$

and approximate the time derivative as

$$\partial_t \mathbf{E}^n \approx \frac{\mathbf{E}^n - \mathbf{E}^{n-1}}{\tau}, \quad \partial_t \mathbf{E}^{n+\frac{1}{2}} \approx \frac{\mathbf{E}^{n+\frac{1}{2}} - \mathbf{E}^n}{\tau/2}. \tag{27}$$

**Remark 1.** For the following formulation of the boundary conditions

$$\mathbf{E} \times \hat{n} = 0 \quad \mathbf{H} \cdot \hat{n} = 0 \tag{28}$$

on the cube boundary  $\partial\Omega = \Gamma_1 \cup \Gamma_2 \cup \Gamma_3$ , where  $\hat{n} = \pm \hat{e}_k$  on  $\Gamma_k$ , we have

- $E_2 = E_3 = 0$  on  $\Gamma_1$ ,
- $E_1 = E_3 = 0$  on  $\Gamma_2$ ,
- $E_1 = E_2 = 0$  on  $\Gamma_3$ .

In this case, the boundary conditions indeed vanish. However, these boundary conditions reflect waves and are unsuitable for simulating a purely wave propagation problem.

#### 4. Full formulation of the time-dependent Maxwell's equations with absorbing boundary conditions suitable for variational splitting

The full variational splitting scheme is the following

$$b_{\alpha\beta}(u, v) = \lambda \langle \partial_\alpha u, \partial_\beta v \rangle \quad a_\alpha(u, v) = \langle u, v \rangle + b_{\alpha\alpha}(u, v), \tag{29}$$

$$c_\alpha(\mathbf{F}, v) = \frac{\tau}{2\epsilon} \langle (\nabla \times \mathbf{F})_\alpha, v \rangle \quad \gamma_\alpha(u, v) = \lambda \mu \langle u, v \rangle_{\Gamma_\alpha},$$

When going from time step  $n$  to time step  $n + \frac{1}{2}$ , we have the values of the electric field  $E_1^n, E_2^n, E_3^n$ . We also have the magnetic field  $\mathbf{H}^n$  computed at previous time step. In the next sub-step, we compute updates  $E_1^{n+\frac{1}{2}}, E_2^{n+\frac{1}{2}}$ , and  $E_3^{n+\frac{1}{2}}$ ,

$$a_2(E_1^{n+\frac{1}{2}}, v) = (E_1^n, v) + b_{12}(E_2^n, v) + c_1(\mathbf{H}^n, v) - \gamma_2 \left( \frac{\partial U_1}{\partial t} + \frac{1}{\eta} \partial_t E_1^n, v \right),$$

$$a_3(E_2^{n+\frac{1}{2}}, v) = (E_2^n, v) + b_{23}(E_3^n, v) + c_2(\mathbf{H}^n, v) - \gamma_3 \left( \frac{\partial U_2}{\partial t} + \frac{1}{\eta} \partial_t E_2^n, v \right),$$

$$a_1(E_3^{n+\frac{1}{2}}, v) = (E_3^n, v) + b_{31}(E_1^n, v) + c_3(\mathbf{H}^n, v) - \gamma_1 \left( \frac{\partial U_3}{\partial t} + \frac{1}{\eta} \partial_t E_3^n, v \right). \tag{30}$$

Now, we also compute  $\mathbf{H}^{n+\frac{1}{2}} = \mathbf{H}^n - \frac{\tau}{2\mu} (C_1 \mathbf{E}^n - C_2 \mathbf{E}^{n+\frac{1}{2}})$  (using equation (6)). When going from time step  $n + \frac{1}{2}$  to time step  $n + 1$ , we already have the values of the electric field  $E_1^{n+\frac{1}{2}}, E_2^{n+\frac{1}{2}}, E_3^{n+\frac{1}{2}}$ . In the next sub-step we compute  $E_1^{n+1}, E_2^{n+1}, E_3^{n+1}$ ,

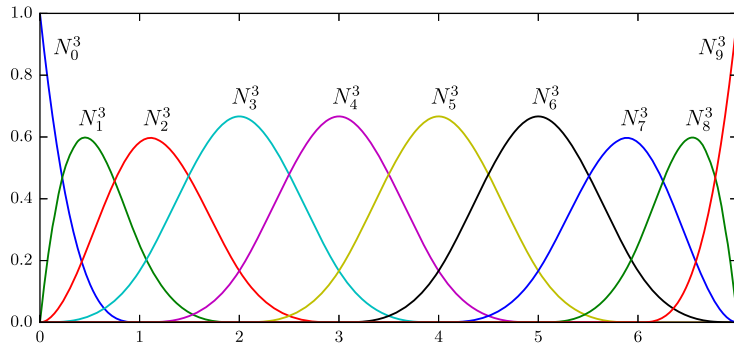


Fig. 1. One dimensional B-spline basis functions.

$$\begin{aligned}
 a_3(\mathbf{E}_1^{n+1}, v) &= \left( E_1^{n+\frac{1}{2}}, v \right) + b_{13}(E_3^{n+\frac{1}{2}}, v) + c_1(\mathbf{H}^{n+\frac{1}{2}}, v) \\
 &\quad - \gamma_3 \left( \frac{\partial U_1}{\partial t} + \frac{1}{\eta} \partial_t E_1^{n+\frac{1}{2}}, v \right), \\
 a_1(\mathbf{E}_2^{n+1}, v) &= \left( E_2^{n+\frac{1}{2}}, v \right) + b_{21}(E_1^{n+\frac{1}{2}}, v) + c_2(\mathbf{H}^{n+\frac{1}{2}}, v) \\
 &\quad - \gamma_1 \left( \frac{\partial U_2}{\partial t} + \frac{1}{\eta} \partial_t E_2^{n+\frac{1}{2}}, v \right), \\
 a_2(\mathbf{E}_3^{n+1}, v) &= \left( E_3^{n+\frac{1}{2}}, v \right) + b_{32}(E_2^{n+\frac{1}{2}}, v) + c_3(\mathbf{H}^{n+\frac{1}{2}}, v) \\
 &\quad - \gamma_2 \left( \frac{\partial U_3}{\partial t} + \frac{1}{\eta} \partial_t E_3^{n+\frac{1}{2}}, v \right). \tag{31}
 \end{aligned}$$

Finally, we compute  $\mathbf{H}^{n+1} = \mathbf{H}^{n+\frac{1}{2}} - \frac{\tau}{2\mu} (C_1 \mathbf{E}^{n+1} - C_2 \mathbf{E}^{n+\frac{1}{2}})$  using equation (7).

5. Discretization with B-spline basis functions

Over the regular domain  $\Omega = [a_1, b_1] \times [a_2, b_2] \times [a_3, b_3]$  we introduce the space  $U_h$  of tensor products of one-dimensional B-splines

$$U_h = \text{span} \{ B_{ijk} : i = 1, \dots, N_1, j = 1, \dots, N_2, k = 1, \dots, N_3 \} \tag{32}$$

where

$$B_{ijk}(\mathbf{x}) = B_i^1(x_1) B_j^2(x_2) B_k^3(x_3) \tag{33}$$

and  $B_i^n$  denotes the one-dimensional B-spline basis functions, see Fig. 1. In the discrete form of (12), we omit boundary terms and we separate directions. We denote B-splines along  $x, y,$  and  $z$  using black, red, and blue colors.

$$(B_{ijk}, B_{pqr}) + \lambda (\partial_2 B_{ijk}, \partial_2 B_{pqr}) = \tag{34}$$

$$\int_{\Omega} B_{ijk} B_{pqr} dx + \lambda \int_{\Omega} \partial_2 B_{ijk} \partial_2 B_{pqr} dx = \tag{35}$$

$$\int_{\Omega} B_i^1 B_j^2 B_k^3 B_p^1 B_q^2 B_r^3 dx + \lambda \int_{\Omega} \partial_2 (B_i^1 B_j^2 B_k^3) \partial_2 (B_p^1 B_q^2 B_r^3) dx = \tag{36}$$

$$\int_{\Omega} (B_i^1 B_p^1) (B_j^2 B_q^2) (B_k^3 B_r^3) dx + \lambda \int_{\Omega} (B_i^1 B_p^1) ((B_j^2)') ((B_q^2)') (B_k^3 B_r^3) dx = \tag{37}$$

$$\left( \int_{\Omega_1} B_i^1 B_p^1 dx_1 \right) \left( \int_{\Omega_2} B_j^2 B_q^2 dx_2 \right) \left( \int_{\Omega_3} B_k^3 B_r^3 dx_3 \right) + \tag{38}$$

$$\lambda \left( \int_{\Omega_1} B_i^1 B_p^1 dx_1 \right) \left( \int_{\Omega_2} (B_j^2)' (B_q^2)' dx_2 \right) \left( \int_{\Omega_3} B_k^3 B_r^3 dx_3 \right) = \tag{39}$$

$$\left( \int_{\Omega_1} B_i^1 B_p^1 dx_1 \right) \left( \int_{\Omega_2} B_j^2 B_q^2 + \lambda (B_j^2)' (B_q^2)' dx_2 \right) \left( \int_{\Omega_3} B_k^3 B_r^3 dx_3 \right). \tag{40}$$

where  $\Omega_1 = [a_1, b_1], \Omega_2 = [a_2, b_2]$  and  $\Omega_3 = [a_3, b_3]$ . We can perform the similar decomposition for the other equations (13), (14). Assuming the boundary terms vanish, we are left with

$$\begin{aligned}
 \mathbf{L}^{(1)} &= \mathbf{M}_1 \otimes (\mathbf{M}_2 + \lambda \mathbf{S}_2) \otimes \mathbf{M}_3 \\
 \mathbf{L}^{(2)} &= \mathbf{M}_1 \otimes \mathbf{M}_2 \otimes (\mathbf{M}_3 + \lambda \mathbf{S}_3) \\
 \mathbf{L}^{(3)} &= (\mathbf{M}_1 + \lambda \mathbf{S}_1) \otimes \mathbf{M}_2 \otimes \mathbf{M}_3
 \end{aligned} \tag{41}$$

Here  $\mathbf{M}_\alpha, \mathbf{S}_\alpha$  denotes the one-dimensional mass and stiffness matrices. This Kronecker product structure matrices can be efficiently solved using in a linear  $\mathcal{O}(N)$  computational cost.

6. Numerical examples

In the following, we consider a model to analyze an antenna problem and also a scattering problem. Both problems are open region problems, i.e., the electromagnetic field is non-zero in an unbounded region. Nevertheless, in order for the discretization of the mathematical model to lead to a finite number of unknowns, the original unbounded domain is truncated resulting in a bounded domain  $\Omega$ . An appropriate boundary condition is used on that external truncation boundary as it is specified below. Thus, considering constant (with time) material data parameters  $\epsilon, \mu,$  we have:

$$\nabla \times \mathbf{E}(\mathbf{r}, t) = -\mathbf{M}_{\text{imp}}(\mathbf{r}, t) - \mu \frac{\partial \mathbf{H}(\mathbf{r}, t)}{\partial t} \quad \mathbf{r} \in \Omega \tag{42}$$

$$\nabla \times \mathbf{H}(\mathbf{r}, t) = \mathbf{J}_{\text{imp}}(\mathbf{r}, t) + \epsilon \frac{\partial \mathbf{E}(\mathbf{r}, t)}{\partial t} \quad \mathbf{r} \in \Omega \tag{43}$$

in which we have that all currents in the model are impressed currents ( $\mathbf{J} = \mathbf{J}_{\text{imp}}, \mathbf{M} = \mathbf{M}_{\text{imp}}$ ).

Denoting  $\partial\Omega_S$  the above mentioned external truncation boundary of  $\Omega$  we will consider<sup>1</sup> the boundary condition (15) presented in Section 3.1 that are repeated here for convenience

$$(-\hat{\mathbf{n}} \times \mathbf{H}(\mathbf{r}, t)) + \frac{1}{\eta} (\hat{\mathbf{n}} \times \hat{\mathbf{n}} \times \mathbf{E}(\mathbf{r}, t)) = \mathbf{E}^{\text{inc}}(\mathbf{r}, t) \quad \mathbf{r} \in \partial\Omega_S, \tag{44}$$

where  $\eta$  is the intrinsic impedance of the medium at  $\partial\Omega_S$  (typically vacuum and hence  $\eta = \eta_0 = \sqrt{\mu_0/\epsilon_0} = 120\pi$ ) and  $U(\mathbf{r}, t)$  is either null or a known function. Symbol  $\hat{\mathbf{n}}$  denotes the outward unit normal to  $\partial\Omega_S$ .

Since boundary conditions (44) introduce coupling between  $\mathbf{E}$  and  $\mathbf{H}$ , they are difficult to use directly with our splitting scheme. We can, however, reformulate them in terms of either only  $\mathbf{E}$  or only  $\mathbf{H}$ :

$$\left( \hat{\mathbf{n}} \times \frac{1}{\mu} \nabla \times \mathbf{E}(\mathbf{r}, t) \right) + \frac{1}{\eta} \left( \hat{\mathbf{n}} \times \hat{\mathbf{n}} \times \frac{\partial \mathbf{E}(\mathbf{r}, t)}{\partial t} \right) = \frac{\partial \mathbf{U}(\mathbf{r}, t)}{\partial t} \quad \mathbf{r} \in \partial\Omega_S \tag{45}$$

<sup>1</sup> Later we elaborate with other possible boundary conditions in given cases.

$$\left(\hat{\mathbf{n}} \times \frac{1}{\varepsilon} \nabla \times \mathbf{H}(\mathbf{r}, t)\right) + \eta \left(\hat{\mathbf{n}} \times \hat{\mathbf{n}} \times \frac{\partial \mathbf{H}(\mathbf{r}, t)}{\partial t}\right) = \frac{\partial \mathbf{U}(\mathbf{r}, t)}{\partial t} \quad \mathbf{r} \in \partial\Omega_S \quad (46)$$

The initial conditions for the field are homogeneous:

$$\mathbf{E}(\mathbf{r}, 0) = 0, \quad \mathbf{H}(\mathbf{r}, 0) = 0 \quad (47)$$

Thus, the excitation of the problem comes from the excitation currents

$$\mathbf{J}_{\text{imp}}(\mathbf{r}, t) = \mathbf{J}_{\text{imp}}^0(\mathbf{r}, t) \neq 0 \quad (48)$$

$$\mathbf{M}_{\text{imp}}(\mathbf{r}, t) = \mathbf{M}_{\text{imp}}^0(\mathbf{r}, t) \neq 0 \quad (49)$$

and/or from the non-zero value of  $\mathbf{U}(\mathbf{r}, t)$

$$\mathbf{U}(\mathbf{r}, t) = \mathbf{U}^0(\mathbf{r}, t) \neq 0 \quad (50)$$

We assume that all the excitations are strictly inside the domain, so  $\mathbf{J}_{\text{imp}}$  and  $\mathbf{M}_{\text{imp}}$  are zero at the boundary. With this assumption, the derivation of the absorbing boundary conditions remains valid, since at/near the boundary the equations retain the original form (without the excitations).

### 6.1. Scattering of a plane wave in $\hat{\mathbf{z}}$

In this example, we analyze the problem of the scattering of an incident plane wave ( $\mathbf{E}^{\text{inc}}, \mathbf{H}^{\text{inc}}$ ) in a vacuum region (i.e.,  $\varepsilon = \varepsilon_0, \mu = \mu_0$ ). As there is not any scatter, the solution to this problem is:

$$\mathbf{E} = \mathbf{E}^{\text{inc}}, \quad \mathbf{H} = \mathbf{H}^{\text{inc}} \quad (51)$$

Thus, this example serves as an initial test of the Absorbing Boundary Condition implemented in the code. We use incident plane waves propagating in a direction perpendicular to one of the faces of the unit square domain, and the electric and magnetic field components are parallel to its sides. For instance, we choose the plane wave to incide from below, i.e., a plane wave propagating on  $+\hat{\mathbf{z}}$  direction and inciding on horizontal face  $z = 0$  of the domain from “below”. Thus,

$$\mathbf{E}^{\text{inc}}(z, t) = E_0 \cos\left(\omega_0\left(t - \frac{z}{c_0}\right)\right) g\left(t - \frac{z}{c_0}\right) \hat{\mathbf{x}} \quad (52)$$

$$\mathbf{H}^{\text{inc}}(z, t) = \frac{E_0}{\eta_0} \cos\left(\omega_0\left(t - \frac{z}{c_0}\right)\right) g\left(t - \frac{z}{c_0}\right) \hat{\mathbf{y}} \quad (53)$$

where  $k_0/\omega_0 = c_0$ ,  $k_0$  is a wave number (can be chosen freely to fix frequency), and any value for  $E_0$  can be chosen, e.g.,  $E_0 = 1$ . The function  $g(t)$  can be chosen in different ways, e.g., Gaussian pulse as defined later. It can easily be shown that the incident field given by expressions (52)-(53) is a solution of Maxwell’s Equations (42)–(43). It can also be shown that they satisfy the boundary conditions (44), (45) and (46). Now, we will show how to define  $\mathbf{W}(z, t) = \frac{\partial \mathbf{U}(z, t)}{\partial t}$  of the boundary condition (45) so this manufactured solution is satisfied. Let us consider first (45), specifically in vacuum medium, i.e.,  $\mu = \mu_0, \eta = \eta_0$ .

$$\left(\hat{\mathbf{n}} \times \frac{1}{\mu_0} \nabla \times \mathbf{E}^{\text{inc}}(z, t)\right) + \frac{1}{\eta_0} \left(\hat{\mathbf{n}} \times \hat{\mathbf{n}} \times \frac{\partial \mathbf{E}^{\text{inc}}(z, t)}{\partial t}\right) = \frac{\partial \mathbf{U}(z, t)}{\partial t} = \mathbf{W}(z, t) \quad (54)$$

As  $\nabla \times \mathbf{E}^{\text{inc}}(z, t) = \hat{\mathbf{z}} \times \partial \mathbf{E}^{\text{inc}}(z, t) / \partial z$ , we have

$$\begin{aligned} \frac{1}{\mu_0} \nabla \times \mathbf{E}^{\text{inc}}(\mathbf{r}, t) &= \frac{1}{\mu_0} \hat{\mathbf{z}} \times \frac{\partial \mathbf{E}^{\text{inc}}(z, t)}{\partial z} \\ &= \hat{\mathbf{y}} \frac{E_0}{\mu_0} \left[ \frac{\omega_0}{c_0} \sin\left(\omega_0\left(t - \frac{z}{c_0}\right)\right) g\left(t - \frac{z}{c_0}\right) \right. \\ &\quad \left. - \frac{1}{c_0} \cos\left(\omega_0\left(t - \frac{z}{c_0}\right)\right) g'\left(t - \frac{z}{c_0}\right) \right] \end{aligned} \quad (55)$$

On the other hand,

$$\frac{\partial \mathbf{E}^{\text{inc}}(z, t)}{\partial t} = \hat{\mathbf{x}} E_0 \left[ -\omega_0 \sin\left(\omega_0\left(t - \frac{z}{c_0}\right)\right) g\left(t - \frac{z}{c_0}\right) \right.$$

$$\left. + \cos\left(\omega_0\left(t - \frac{z}{c_0}\right)\right) g'\left(t - \frac{z}{c_0}\right) \right] \quad (56)$$

For simplicity, we define

$$\begin{aligned} A(z, t) &= \omega_0 \sin\left(\omega_0\left(t - \frac{z}{c_0}\right)\right) g\left(t - \frac{z}{c_0}\right) \\ &\quad - \cos\left(\omega_0\left(t - \frac{z}{c_0}\right)\right) g'\left(t - \frac{z}{c_0}\right) \end{aligned} \quad (57)$$

so we can write

$$\frac{1}{\mu_0} \nabla \times \mathbf{E}^{\text{inc}}(z, t) = \hat{\mathbf{y}} \frac{E_0}{\mu_0 c_0} A(z, t) = \hat{\mathbf{y}} \frac{E_0}{\eta_0} A(z, t) \quad (58)$$

$$\frac{\partial \mathbf{E}^{\text{inc}}(z, t)}{\partial t} = -\hat{\mathbf{x}} E_0 A(z, t) \quad (59)$$

Let us now check how the boundary condition (54) using (58), (59) looks at the faces of the unit cube domain:

- Face  $z = 0$ :  $\hat{\mathbf{n}} = -\hat{\mathbf{z}}$  and  $\mathbf{W}(0, t) = 2 \frac{E_0 \hat{\mathbf{x}}}{\eta_0} A(0, t)$
- Face  $z = 1$ :  $\hat{\mathbf{n}} = \hat{\mathbf{z}}$  and  $\mathbf{W}(1, t) = 0$
- Faces  $y = 0, 1$ :  $\hat{\mathbf{n}} = \mp \hat{\mathbf{y}}$  and  $\mathbf{W}(z, t) = \frac{E_0 \hat{\mathbf{x}}}{\eta_0} A(z, t)$
- Faces  $x = 0, 1$ :  $\hat{\mathbf{n}} = \mp \hat{\mathbf{x}}$  and  $\mathbf{W}(z, t) = \mp \frac{E_0 \hat{\mathbf{z}}}{\eta_0} A(z, t)$

See Appendix A for a detailed computation.

#### Remarks.

1. For faces perpendicular to  $\hat{\mathbf{z}}$  (i.e., to the direction of propagation of the wave) we observe that both terms of the left hand side of the boundary condition (54) are non null. In other words, (54) is acting (as expected) as a impedance boundary condition.
2. Note that for  $z = 0, 1$  both terms of the left hand side of the boundary condition (54) have the same magnitude (they either sum up or cancel out).
3. Specifically, for face  $z = 0$  the wave is going inwards (from outside to inside of the domain) and  $\mathbf{W}(0, t) \neq 0$ . On the other hand, for face  $z = 1$  the wave is going outwards (from inside to outside of the domain) and, hence,  $\mathbf{W}(0, t) = 0$ .
4. In contrary, for the other faces (those not perpendicular to  $\hat{\mathbf{z}}$ ), (54) is not acting as a impedance boundary condition but rather as Dirichlet or Neumann boundary conditions. Note that one of the two terms of the left hand side of the boundary condition (54) is null. This corresponds to the case of no power flowing either inwards or outwards of the domain through these faces.
5. For faces  $y = 0, 1$  we have the prescription of Dirichlet type boundary conditions in a weak sense.
6. For faces  $x = 0, 1$  we have the prescription of Neumann type boundary conditions in a weak sense.

The same steps that have been taken to show the satisfaction of (45) by the incident field can be made, in an analogous fashion, for (46). If we do it, we expect

1. For faces  $z = 0, 1$  we obtain dual (changing  $\eta$  by  $1/\eta$ , and  $\hat{\mathbf{x}}$  by  $\hat{\mathbf{y}}$ ) results to those of (A.1) and (A.2), respectively.
2. For the other faces we also recover Dirichlet type and Neumann type boundary conditions but interchanging faces  $x = \text{constant}$  and  $y = \text{constant}$ . That is, we obtain a Dirichlet type boundary condition for faces  $x = 0, 1$  and a Neumann type boundary condition for faces  $y = 0, 1$ .

For discretization we use a mesh size of  $4 \times 4 \times 100$  elements, quadratic B-splines, and the time step  $\tau = 2.5 \times 10^{-11}$ . We perform 4000 steps of the simulation to observe the traverse of the gener-

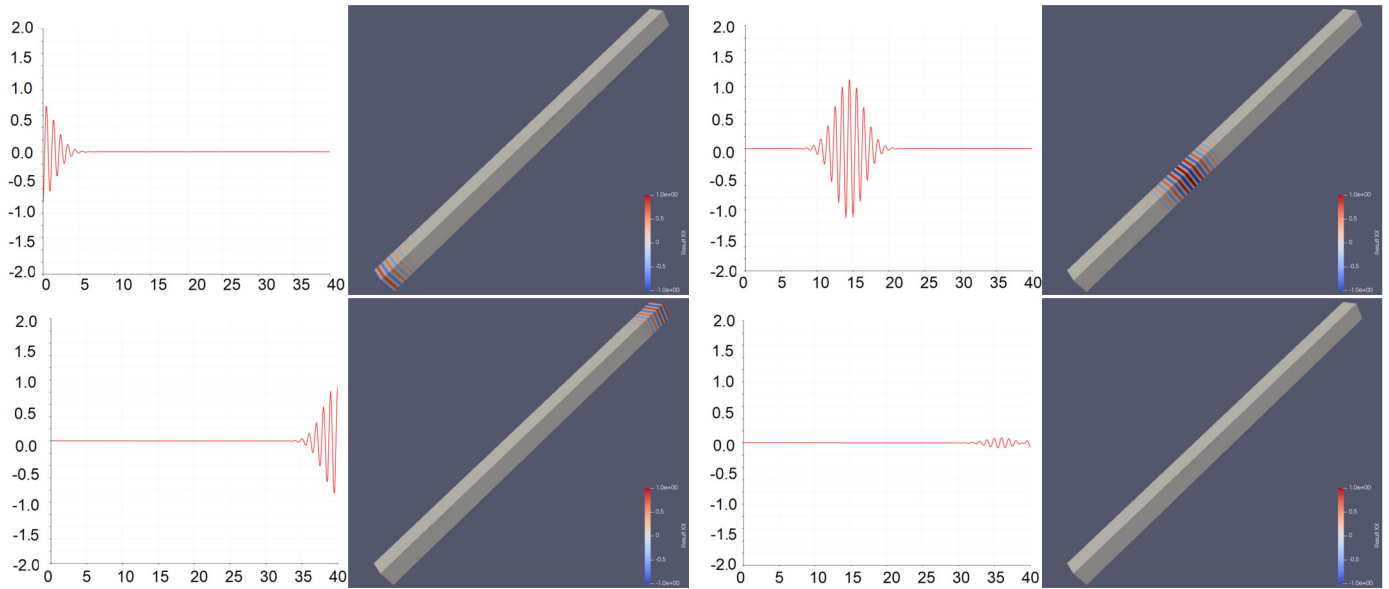


Fig. 2. Values of the  $x$  component of the electric field  $E$  [V/m] at time steps 500, 1500, 3200, 3500. They correspond to the time moments  $t = 12.5[ns], 37.5[ns], 80[ns], 87.5[ns]$ .

ated pulse. The total time of the simulation is  $100[ns]$ . Here,  $g(t) = \exp\left(-\frac{1}{2} \left(\frac{t-t_0}{\tau}\right)^2\right)$  for  $t > 0$ , and 0 otherwise, with  $t_0 = 4\tau$  and  $\tau = 2\pi/\omega$ . The numerical results are presented in Fig. 2. The small reflection that we observe results from the finite difference numerical approximation to the time derivative in the boundary conditions employed (45)-(46).

6.2. Radiation problem. Wire antenna problem modeled with its current

The use of Equivalence Principles in electromagnetic field theory [26, chapter 7] allow to model wire antennas by substituting the wires with their electric current density along themselves. For simple wire antennas such as the electric dipoles, the equivalent current density can very well approximated by a constant (with space) density current  $\mathbf{J}_{imp}$ . Thus, the problem domain consists of a volume (e.g., a cube) enclosing the current that “acts” as an antenna. The excitation terms of the formulation for this case are  $\mathbf{J}_{imp} \neq 0$  and  $\mathbf{M}_{imp} = 0, \mathbf{U} = 0$ . Thus, to model the antenna, we reset the incident wave  $\mathbf{U} = 0$ , and we add an additional term on the right-hand side representing the electric dipole

$$\begin{aligned} \partial_t \mathbf{E} &= \frac{1}{\epsilon_0} \nabla \times \mathbf{H} - \mathbf{J}_{imp} \\ \partial_t \mathbf{H} &= -\frac{1}{\mu_0} \nabla \times \mathbf{E}. \end{aligned} \tag{60}$$

The impressed current  $\mathbf{J}_{imp}$  is non-zero on a very thin, short part of  $\Omega$ .

We simulate the antenna on a cube shape domain  $\Omega = [-1, 1] \times [-1, 1] \times [-1, 1]$  with the impressed current defined as

$$\mathbf{J}_{imp}(\mathbf{x}, t) = \begin{cases} J_0(x_3, t) \hat{\mathbf{e}}_3 & x_1 = x_2 = 0, x_3 \in [-l/2, l/2] \\ 0 & \text{elsewhere} \end{cases} \tag{61}$$

where  $J_0(x, t) = g(t) \sin \omega_0 t$  and

$$g(t) = 1 - \exp(-t/\sigma) \tag{62}$$

with  $l = 1/50, \omega_0 = 2\pi f_0, f_0 = 2c_0$ , and  $\sigma = 2/f_0$ . We employ a mesh with  $100 \times 100 \times 100$  elements with quadratic B-splines. During the simulation, we use a time step  $\tau = 2.5 \times 10^{-11}$ , which corresponds to a total of 400 steps (total simulation time is  $10[ns]$ ). We present the simulation results in Fig. 3. We compare against the analytical solution as discussed in [chapter 12 [22] expression (12.10) and (12.12)], and we observe an agreement between the analytical results and numerical so-

lution. Fig. 4 compares the radial component  $E_r$  of the electric field  $\mathbf{E}$  of the numerical vs. the analytical solution.

6.3. Verification of the order of the time-integration scheme

The goal of the first numerical example is to verify the order of the time-integration scheme. For  $\Omega = (0, 1)^3$ , for  $\epsilon = 1$  and  $\mu = 1$  we define

$$u_{\kappa, \lambda}^1(x, t) = \begin{bmatrix} \sin(\kappa \pi x_2) \sin(\lambda \pi x_3) \cos(\sqrt{\kappa^2 + \lambda^2} \pi t) \\ 0 \\ 0 \\ 0 \\ -\frac{\lambda}{\sqrt{\kappa^2 + \lambda^2}} \sin(\kappa \pi x_2) \cos(\lambda \pi x_3) \sin(\sqrt{\kappa^2 + \lambda^2} \pi t) \\ \frac{\kappa}{\sqrt{\kappa^2 + \lambda^2}} \cos(\kappa \pi x_2) \sin(\lambda \pi x_3) \sin(\sqrt{\kappa^2 + \lambda^2} \pi t) \end{bmatrix} \tag{63}$$

$$u_{\kappa, \lambda}^2(x, t) = \begin{bmatrix} 0 \\ \sin(\kappa \pi x_1) \sin(\lambda \pi x_3) \cos(\sqrt{\kappa^2 + \lambda^2} \pi t) \\ 0 \\ -\frac{\lambda}{\sqrt{\kappa^2 + \lambda^2}} \sin(\kappa \pi x_1) \cos(\lambda \pi x_3) \sin(\sqrt{\kappa^2 + \lambda^2} \pi t) \\ 0 \\ \frac{\kappa}{\sqrt{\kappa^2 + \lambda^2}} \cos(\kappa \pi x_1) \sin(\lambda \pi x_3) \sin(\sqrt{\kappa^2 + \lambda^2} \pi t) \end{bmatrix} \tag{64}$$

$$u_{\kappa, \lambda}^3(x, t) = \begin{bmatrix} 0 \\ 0 \\ \sin(\kappa \pi x_1) \sin(\lambda \pi x_2) \cos(\sqrt{\kappa^2 + \lambda^2} \pi t) \\ -\frac{\lambda}{\sqrt{\kappa^2 + \lambda^2}} \sin(\kappa \pi x_1) \cos(\lambda \pi x_2) \sin(\sqrt{\kappa^2 + \lambda^2} \pi t) \\ \frac{\kappa}{\sqrt{\kappa^2 + \lambda^2}} \cos(\kappa \pi x_1) \sin(\lambda \pi x_2) \sin(\sqrt{\kappa^2 + \lambda^2} \pi t) \\ 0 \end{bmatrix} \tag{65}$$

for  $\kappa, \lambda \in \mathbb{Z}, \kappa, \lambda \neq 0$ .

The first manufactured solution function is

$$\mathbf{u}_A(x, t) = \alpha \left( u_{1,1}^1(x, t) + 2u_{1,1}^2(x, t) + 3u_{1,1}^3(x, t) \right) \tag{66}$$

Notice that  $\mathbf{u}_A$  has six components, where the first three components correspond to  $\mathbf{E}$  and the last three components to  $\mathbf{H}$ . The parameter  $\alpha$  is selected in such a way that  $\|\mathbf{u}_A(x, 0)\|_{L^2(\Omega)} = 1$ . Since

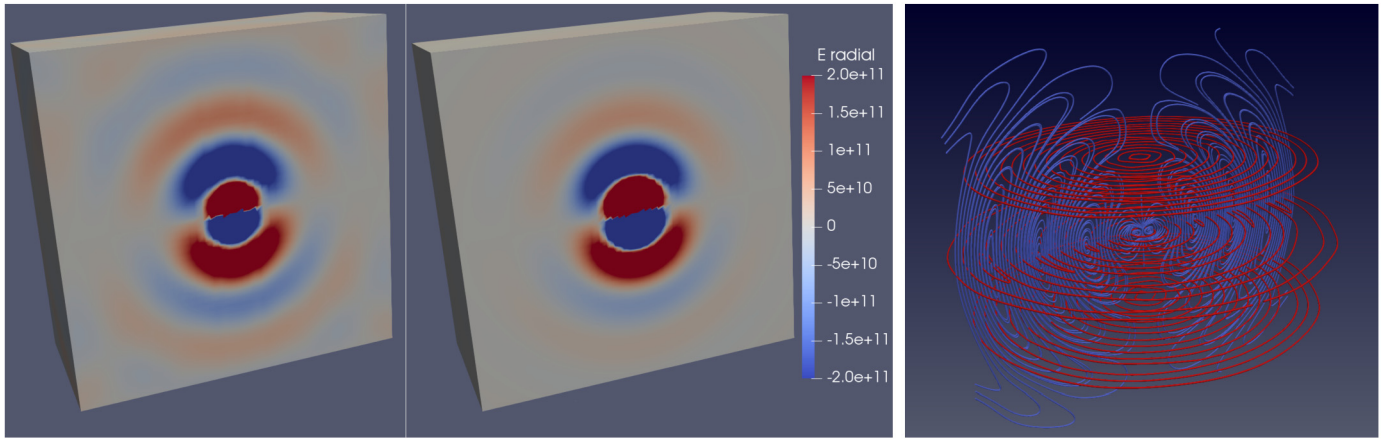


Fig. 3. Comparison of the numerical solution to the dipole antenna problem (left panel) and the exact solution (analytical solution) (central panel). The plots present the radial component of the electric field  $E$  [V/m]. Electric and magnetic fields streamlines (right panel). Snapshot from time step 230.

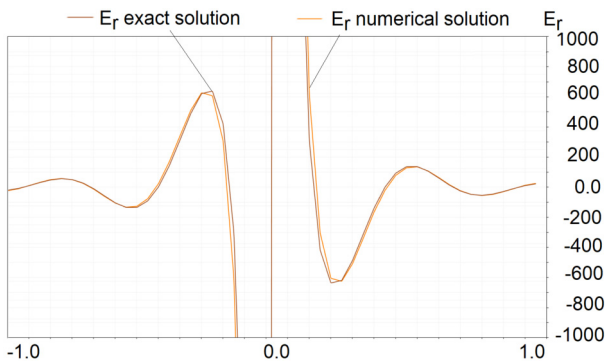


Fig. 4. Illustration on how radial components of electric field  $E$  [V/m] agree (numerical result and analytical solution). Cross-section at  $x = 0.0, y = 0.0$  and  $z = [-1, 1]$ .

$$\begin{aligned}
 u_{1,1}^1(x, 0) &= \begin{bmatrix} \sin(\pi x_2) \sin(\pi x_3) \\ 0 \\ 0 \\ 0 \\ 0 \\ 0 \end{bmatrix} & u_{1,1}^2(x, 0) &= \begin{bmatrix} 0 \\ \sin(\pi x_1) \sin(\pi x_3) \\ 0 \\ 0 \\ 0 \\ 0 \end{bmatrix} & u_{1,1}^3(x, 0) &= \begin{bmatrix} 0 \\ 0 \\ \sin(\pi x_1) \sin(\pi x_2) \\ 0 \\ 0 \\ 0 \end{bmatrix}
 \end{aligned} \tag{67}$$

we have

$$\begin{aligned}
 \|\mathbf{u}_A(x, 0)\|_{L^2(\Omega)}^2 &= (\mathbf{u}_A(x, 0), \mathbf{u}_A(x, 0)) \\
 &= \int_{(0,1)^3} (\alpha^2 \sin^2(\pi x_2) \sin^2(\pi x_3) + 4\alpha^2 \sin^2(\pi x_1) \sin^2(\pi x_3) \\
 &\quad + 9\alpha^2 \sin^2(\pi x_1) \sin^2(\pi x_2)) dx_1 dx_2 dx_3 = \frac{1}{4}\alpha^2 + \alpha^2 + \frac{9}{4}\alpha^2
 \end{aligned} \tag{68}$$

since  $\int_{(0,1)} \sin^2(\pi x_i) dx_i = \frac{1}{2}$ . We want  $\frac{14}{4}\alpha^2 = 1$ , so  $\alpha = \sqrt{\frac{4}{14}} = \frac{2}{\sqrt{14}}$ .

Fig. 5 shows a numerical verification of the second order implicit second-order time integration scheme. This experiment is performed on a mesh of  $16 \times 16 \times 16$  elements, and we can see that the spatial discretization error dominates around  $10^{-2}$ . In order to further verify the second order of the time integration scheme, we execute the experiments on the computational mesh of  $32 \times 32 \times 32$  elements, as illustrated in Fig. 6. Based on these numerical experiments, we conclude that changing the time step size from  $1/10$  into  $1/640$  does not alter the stability of the method.

#### 6.4. Magnetotelluric measurements simulations

We consider a model magnetotelluric MT problem with the source representing the radiation of the ionosphere.

$$\begin{aligned}
 \partial_t \mathbf{E} &= \frac{1}{\epsilon_0} (\nabla \times \mathbf{H} - \sigma \mathbf{E} - \mathbf{J}_{\text{imp}}) \\
 \partial_t \mathbf{H} &= -\frac{1}{\mu_0} \nabla \times \mathbf{E},
 \end{aligned} \tag{69}$$

where  $\epsilon_0, \mu_0$  are the electric permittivity and magnetic permeability of vacuum,  $\mathbf{J}_{\text{imp}}$  is the source representing the radiation of the ionosphere, and the conduction term  $\sigma \mathbf{E}$  describes the induced currents inside the medium (atmosphere or rock). For this application, we assume isotropic materials, where conductivity  $\sigma = \sigma$  is a scalar given by

$$\sigma = \begin{cases} \sigma_1 & \text{in the ground} \\ \sigma_{\text{air}} & \text{in the atmosphere} \end{cases} \tag{70}$$

where regions of the domain are presented in Fig. 7, and  $\sigma_{\text{air}} = 10^{-10}$ , and  $\sigma_1 \in \{1, 0.1, 0.001\}$ , depending on the simulation run. The source is modeled as a pulse  $\mathbf{J}_{\text{imp}}(t) = \mathbf{J}_0 \delta(t)$  with  $\mathbf{J}_0 = (1, 1, 0)$  in the upper layer of the atmosphere, and  $\mathbf{J}_0 = 0$  elsewhere. We employ the Absorbing Boundary Conditions of the form

$$\hat{\mathbf{n}} \times \frac{1}{\mu} \nabla \times \mathbf{E} + \frac{1}{\eta} \hat{\mathbf{n}} \times (\hat{\mathbf{n}} \times \partial_t \mathbf{E}) = 0 \tag{71}$$

which allows us to construct an efficient splitting time stepping scheme. Our computational domain is  $[0, 600\text{km}] \times [0, 600\text{km}] \times [0, 200\text{km}]$ . The ground is located at  $[0, 600\text{km}] \times [0, 600\text{km}] \times [0, 60\text{km}]$ . We employ a mesh of dimension  $360 \times 360 \times 120$  (total of 15,552,000 elements). The memory required to run our simulation can be estimated in the following way:

$$\begin{aligned}
 &360 \times 360 \times 120[\text{mesh}] \times 6[\text{fields}] \times 8[\text{double precision}] \times 2[\text{previous step}] \\
 &= 2 \text{ GB RAM},
 \end{aligned}$$

a total of 200 GB disc space [every 10th step recorded] for 100 time steps. The snapshots from the transient MT simulations are presented in Fig. 8.

We run the transient Maxwell simulation and we recover the conductivity using the following procedure. For this problem, we record the solution at the receiver antenna, compute the Fast Fourier Transform (FFT) of the  $\mathbf{E}_x$  (electric) and  $\mathbf{H}_y$  (magnetic) field components, compute  $(\text{FFT}(\mathbf{E}_x)/\text{FFT}(\mathbf{H}_y))^2$ , and recover the conductivity  $\sigma = 0.1$  in the frequency domain (see Fig. 9).



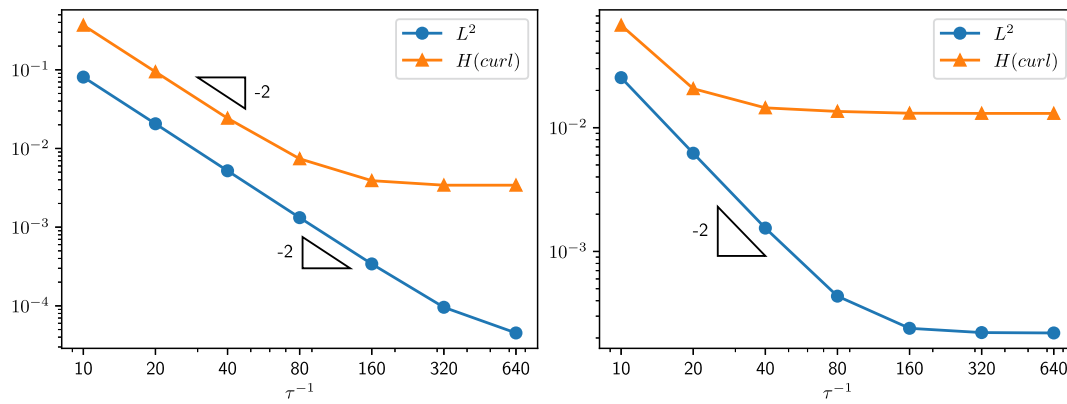


Fig. 5. Convergence in time step size using  $L^2$  and  $H^1(\text{curl})$  norm for the electric (left) and magnetic (right) field. The problem with manufactured solution over the computational mesh with  $16^3$  elements.

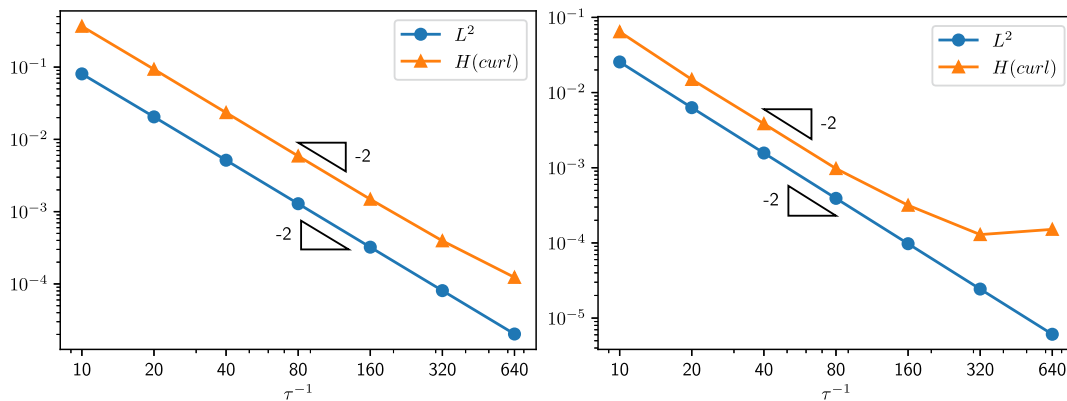


Fig. 6. Convergence in time step size using  $L^2$  and  $H^1(\text{curl})$  norm for the electric (left) and magnetic (right) field. The problem with manufactured solution over the computational mesh with  $64^3$  elements.

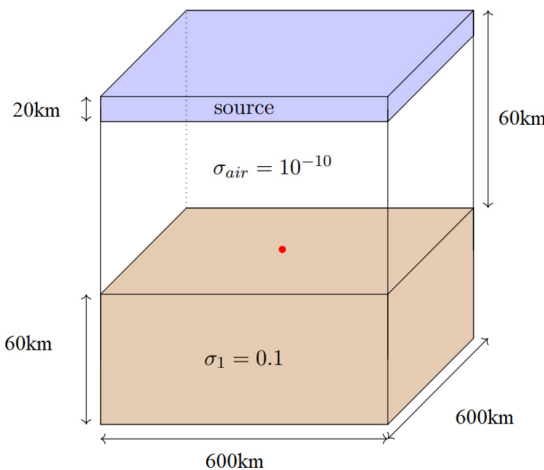


Fig. 7. Prototype of the transient Maxwell code correctly identifies the conductivity of the formation  $\sigma = 0.1$ .

### 7. Parallel scalability

In this section we study the parallel scalability of the solver summarized in Algorithm 1. The presented Algorithm 1 illustrates the computations performed from time step  $n$  into  $n + \frac{1}{2}$  (computing  $\mathbf{E}^{n+\frac{1}{2}}$ ,  $\mathbf{H}^{n+\frac{1}{2}}$  based on  $\mathbf{E}^n$  and  $\mathbf{H}^n$ ) The algorithm performing the computations from time step  $n + \frac{1}{2}$  into  $n + 1$  (computing  $\mathbf{E}^n$  and  $\mathbf{H}^n$  based on  $\mathbf{E}^{n+\frac{1}{2}}$ ,  $\mathbf{H}^{n+\frac{1}{2}}$ ) are similar (compare equations 30 and 31).

The experiments have been performed on a Linux workstation equipped with AMD Ryzen 9 3900X processor with 12 physical cores, and a total 24 virtual cores, running at stock configuration of CPU. The workstation was equipped with 64 GB of RAM, in two dual-channel DDR4 sticks (Corsair Vengeance LPX, 2x32 GB, 3200 MHz, CL16).

The workstation was running openSUSE Leap 15.4, with stock gcc compiler set, version 7.5.0. IGA-ADS was compiled with FMT 8.1.1, GALOIS 6.0.0, MUMPS 5.3.3, LAPACK 3.9.0, ScaLAPACK 2.1.0, boost 1.74.0, METIS 5.1.0, mpich 3.3.2, and Lyra 1.6. All computations were performed by executing the code in shared memory only.

For each of the governing equations (30)–(31) we perform the parallel generation of the right-hand side vector. We report in Figs. 10–12 the execution times of the parallel shared-memory algorithm, over a patch of  $8 \times 8 \times 8$ ,  $16 \times 16 \times 16$ ,  $32 \times 32 \times 32$ ,  $64 \times 64 \times 64$ ,  $128 \times 128 \times 128$ , and  $256 \times 256 \times 256$  elements. We employ 1, 2, 4, 8, 12, 16, and 24 cores. We perform our measurements for linear, quadratic and cubic B-splines.

We also report in Figs. 13–15 the speedup of the parallel shared-memory algorithm, over patches of  $8^3$ ,  $16^3$ ,  $32^3$ ,  $64^3$ ,  $128^3$ , and  $256^3$  elements. We employ 1, 2, 4, 8, 12, 16, or 24 cores. We perform our measurements for linear, quadratic and cubic B-splines.

Finally, in Fig. 16 we report the weak scalability of the parallel shared-memory algorithm, over the patch of  $8 \times 8 \times 8$  elements per core. We perform our measurements for linear, quadratic, and cubic B-splines.

### 8. Conclusions

We derived a linear computational cost simulator for transient Maxwell’s equations. It employs the alternating directions solver and implicit time integration scheme following a rotation operator splitting

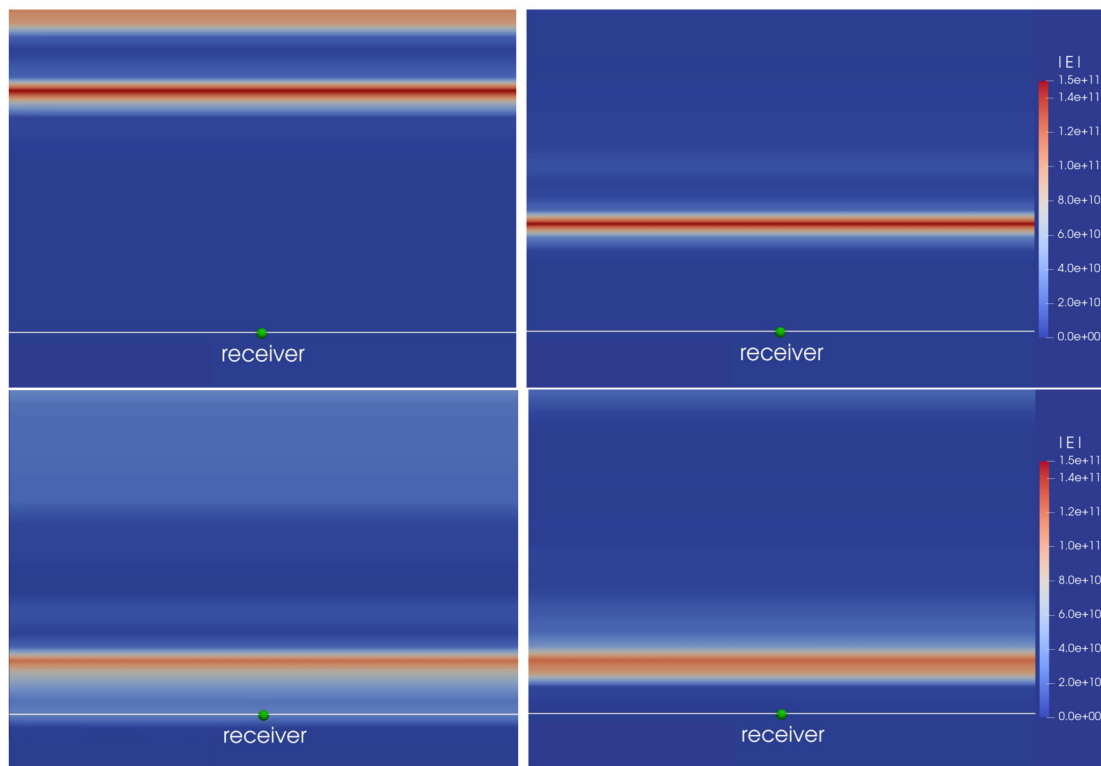


Fig. 8. Snapshots from the simulation – magnitude  $\|E\|$  of the electric field [V/m].

for each element  $K = [\xi_{l_x}, \xi_{r_x+1}] \times [\xi_{l_y}, \xi_{r_y+1}] \times [\xi_{l_z}, \xi_{r_z+1}]$  in parallel do

```

     $U^{loc} \leftarrow 0$ ;
    for each quadrature point  $\xi = (X_{k_x}, X_{k_y}, X_{k_z})$  do
         $\mathbf{x} \leftarrow \Psi_K(\xi)$ ;
         $W \leftarrow w_{k_x} w_{k_y} w_{k_z}$ ;
         $E_1^n, E_2^n, E_3^n \leftarrow 0$ ;
         $E_1^{n+\frac{1}{2}}, E_2^{n+\frac{1}{2}}, E_3^{n+\frac{1}{2}} \leftarrow 0$ ;
         $\mathbf{H}^n, \mathbf{H}^{n+\frac{1}{2}} \leftarrow 0$ ;
        for  $I \in I(K)$  do
             $E_1^n \leftarrow E_1^n + E_{1,I}^n B_I(\xi)$ ;
             $E_2^n \leftarrow E_2^n + E_{2,I}^n B_I(\xi)$ ;
             $E_3^n \leftarrow E_3^n + E_{3,I}^n B_I(\xi)$ ;
             $\mathbf{H}^n \leftarrow \mathbf{H}^n + \mathbf{H}_I^n B_I(\xi)$ ;
        end
        for  $I \in I(K)$  do
             $v \leftarrow B_I(\xi)$ ;
             $E_{1,I}^{n+\frac{1}{2} : loc} \leftarrow E_{1,I}^{n+\frac{1}{2} : loc} +$ 
                 $W |K| \left( (E_1^n, v) + b_{12}(E_2^n, v) + c_1(\mathbf{H}^n, v) - \gamma_2 \left( U_1 + \frac{1}{\eta} \partial_t E_1^n, v \right) \right)$ ;
             $E_{2,I}^{n+\frac{1}{2} : loc} \leftarrow E_{2,I}^{n+\frac{1}{2} : loc} +$ 
                 $W |K| \left( (E_2^n, v) + b_{23}(E_3^n, v) + c_2(\mathbf{H}^n, v) - \gamma_3 \left( U_2 + \frac{1}{\eta} \partial_t E_2^n, v \right) \right)$ ;
             $E_{3,I}^{n+\frac{1}{2} : loc} \leftarrow E_{3,I}^{n+\frac{1}{2} : loc} +$ 
                 $W |K| \left( (E_3^n, v) + b_{31}(E_1^n, v) + c_3(\mathbf{H}^n, v) - \gamma_1 \left( U_3 + \frac{1}{\eta} \partial_t E_3^n, v \right) \right)$ ;
        end
    end
    synchronized
    for  $I \in I(K)$  do
         $E_{1,I}^{n+\frac{1}{2}} \leftarrow E_{1,I}^{n+\frac{1}{2}} + E_{1,I}^{n+\frac{1}{2} : loc}$ ;
         $E_{2,I}^{n+\frac{1}{2}} \leftarrow E_{2,I}^{n+\frac{1}{2}} + E_{2,I}^{n+\frac{1}{2} : loc}$ ;
         $E_{3,I}^{n+\frac{1}{2}} \leftarrow E_{3,I}^{n+\frac{1}{2}} + E_{3,I}^{n+\frac{1}{2} : loc}$ ;
    end
end
end

```

Algorithm 1: Parallel shared-memory solver algorithm. The parallel parts are denoted using blue color.

technique. We also showed that we could incorporate the Absorbing Boundary Condition (ABC) into the linear computational cost solver. We verified the solver’s correctness experimentally using the analytical solution for the dipole antenna. We confirmed the second order of the implicit time integration scheme using the manufactured solution technique. We checked the properties of the ABC formulation using the simulation of the traveling pulse wave. Additionally, we showed that the method could be employed for the simulations of the magnetotelluric measurement process. We implemented our transient Maxwell simulator in the IGA-ADS open-source code. The GALOIS library managed the parallelization of the code. We performed the experimental verification of the weak and strong scalability of the parallel code on a shared-memory Linux cluster node. We showed good performance up to 26 cores. Our simulator can perform transient Maxwell simulations with 15 million finite elements and 100-time steps on a multi-core laptop within several hours.

**Data availability**

Data will be made available on request.

**Acknowledgements**

The work of Marcin Łoś, Maciej Woźniak and Maciej Paszyński has been supported by The European Union’s Horizon 2020 Research and Innovation Program of the Marie Skłodowska-Curie grant agreement No. 777778, MATHROCKS. Scientific paper published within the framework of an international project co-financed with funds from the program of the Ministry of Science and Higher Education entitled “PMW” in years 2022-2023; contract no. 5243/H2020/2022/2. Research project partly supported by program “Excellence initiative – research university” for the AGH University of Science and Technology. David Pardo has received funding from: the European Union’s Horizon 2020 research and innovation program under the Marie Skłodowska-Curie grant agreement No 777778 (MATHROCKS); the Spanish Ministry

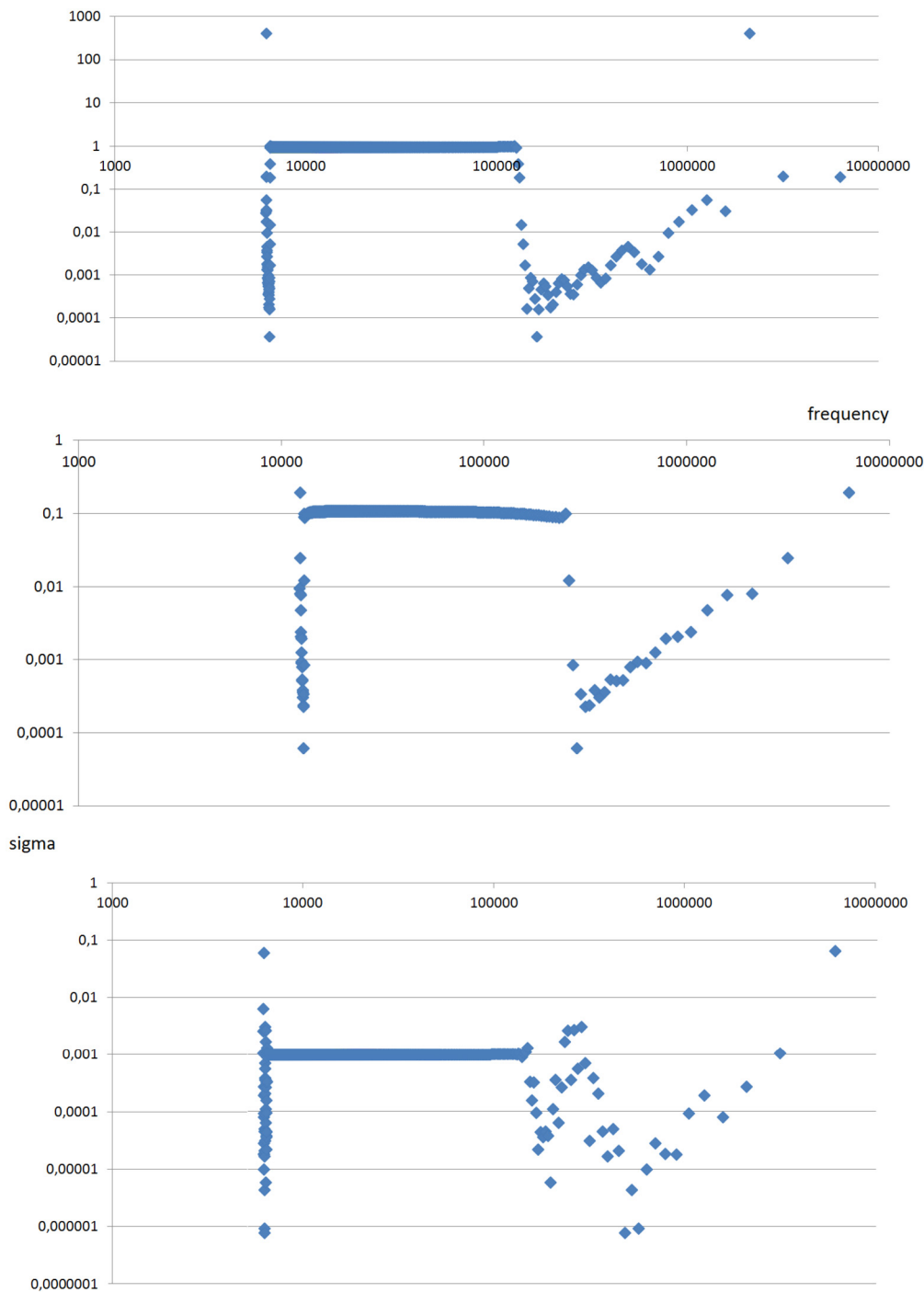


Fig. 9. The conductivity of the formation as restored by the transient Maxwell code, for  $\sigma = 1, 0.1, 0.001$ .

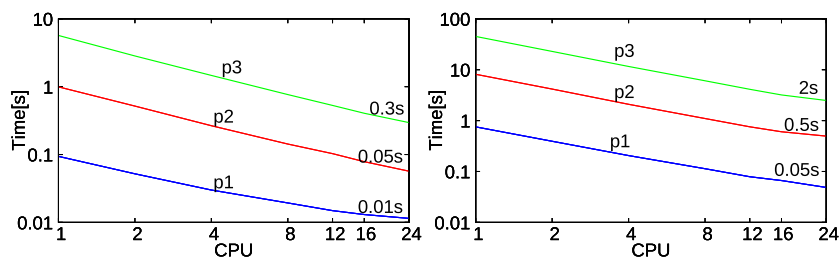


Fig. 10. Execution time over the computational mesh of size  $8 \times 8 \times 8$  elements (left panel) and  $16 \times 16 \times 16$  elements (right panel), for a number of cores = 1, 2, 4, 8, 16, 24 for linear, quadratic and cubic B-splines.

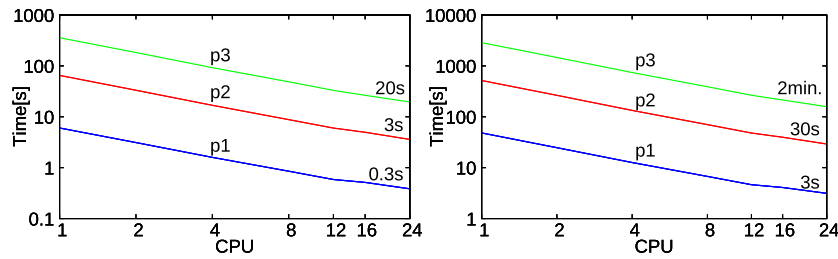


Fig. 11. Execution time over the computational mesh of size  $32 \times 32 \times 32$  elements (left panel) and  $64 \times 64 \times 64$  elements (right panel), for a number of cores = 1,2,4,8,16,24 for linear, quadratic and cubic B-splines.

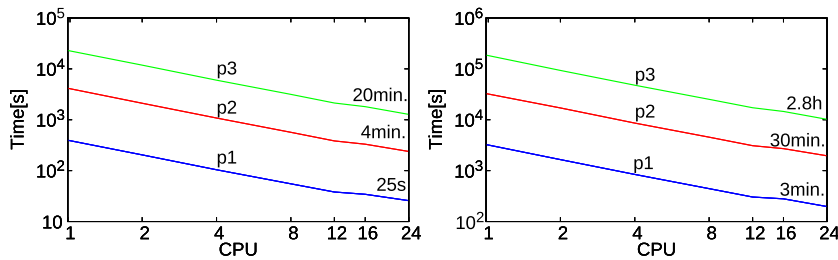


Fig. 12. Execution time over the computational mesh of size  $128 \times 128 \times 128$  elements (left panel) and  $256 \times 256 \times 256$  elements (right panel), for a number of cores = 1,2,4,8,16,24 for linear, quadratic and cubic B-splines.

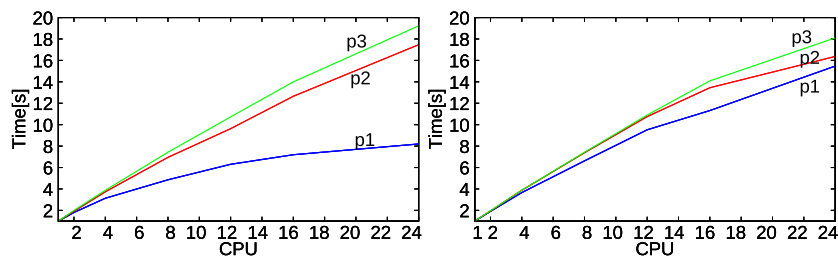


Fig. 13. Speedup over the computational mesh of size  $8 \times 8 \times 8$  elements (left panel) and  $16 \times 16 \times 16$  elements (right panel), for a number of cores = 1,2,4,8,16,24 for linear, quadratic and cubic B-splines.

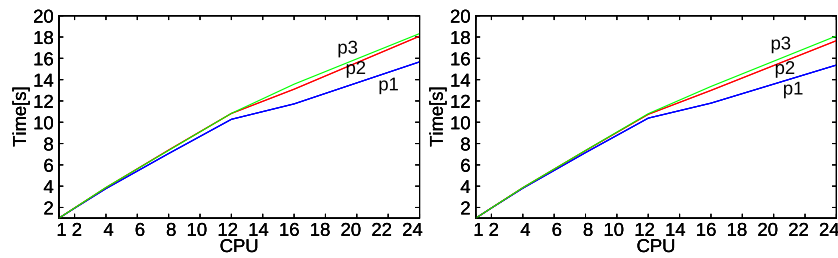


Fig. 14. Speedup over the computational mesh of size  $32 \times 32 \times 32$  elements (left panel) and  $64 \times 64 \times 64$  elements (right panel), for a number of cores = 1,2,4,8,16,24 for linear, quadratic and cubic B-splines.

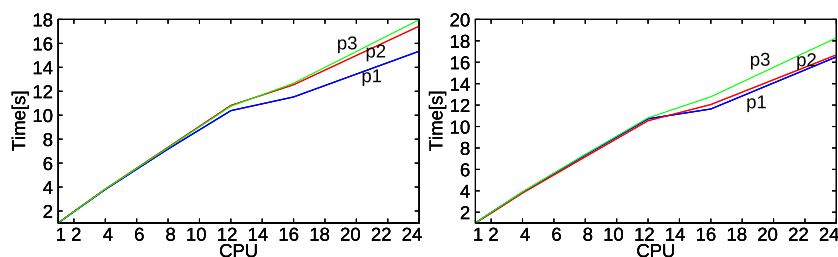


Fig. 15. Speedup over the computational mesh of size  $128 \times 128 \times 128$  elements (left panel) and  $256 \times 256 \times 256$  elements (right panel), for a number of cores = 1,2,4,8,16,24 for linear, quadratic and cubic B-splines.

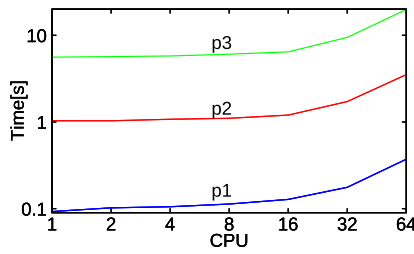


Fig. 16. Weak scalability measured on 1 domain  $8 \times 8 \times 8$  elements per 1 core versus up to 64 subdomains, a total of  $32 \times 32 \times 32$ . Measurements for linear, quadratic and cubic B-splines.

of Science and Innovation projects with references TED2021-132783B-I00, PID2019-108111RB-I00 (FEDER/AEI) and PDC2021-121093-I00 (MCIN / AEI / 10.13039/501100011033/Next Generation EU), the “BCAM Severo Ochoa” accreditation of excellence CEX2021-001142-S / MICIN / AEI / 10.13039/501100011033; and the Basque Government through the BERC 2022-2025 program, the three Elkartek projects 3KIA (KK-2020/00049), EXPERTIA (KK-2021/00048), and SIGZE (KK-2021/00095), and the Consolidated Research Group MATH-MODE (IT1456-22) given by the Department of Education.

The work of Luis E. Garcia-Castillo has been partially supported by Ministerio de Ciencia e Innovación, Gobierno de España (project PID2019-109984RB-C41) as well by the Regional Government of Madrid throughout the project MIMACUHSAPCE-CM-UC3M. Julen Alvarez-Aramberri has received funding from: the European Union-Next GenerationEU, the Euskampus Foundation through the ORLEG-IA project in the Misiones Euskampus 2.0 program, and the European Union’s Horizon 2020 research and innovation program under the Marie Skłodowska-Curie grant agreement No 777778 (MATHROCKS).

### Appendix A. Boundary conditions on a unit cube domain

Let us now check how the boundary condition (54) using (58), (59) looks at the faces of the unit square domain:

- Face  $z = 0$ . We have  $\hat{\mathbf{n}} = -\hat{\mathbf{z}}$ .

$$\begin{aligned} & \left(-\hat{\mathbf{z}} \times \frac{1}{\mu_0} \nabla \times \mathbf{E}^{\text{inc}}(0, t)\right) + \frac{1}{\eta_0} \left(-\hat{\mathbf{z}} \times -\hat{\mathbf{z}} \times \frac{\partial \mathbf{E}^{\text{inc}}(0, t)}{\partial t}\right) = \mathbf{W}(0, t) \\ & \left(\underbrace{(-\hat{\mathbf{z}} \times \hat{\mathbf{y}})}_{\hat{\mathbf{x}}} \frac{E_0}{\eta_0} A(0, t)\right) + \frac{1}{\eta_0} \left(\underbrace{(-\hat{\mathbf{z}} \times -\hat{\mathbf{z}} \times -\hat{\mathbf{x}})}_{\hat{\mathbf{x}}} E_0 A(0, t)\right) = \mathbf{W}(0, t) \\ & \boxed{\mathbf{W}(0, t)} = \boxed{2 \frac{E_0 \hat{\mathbf{x}}}{\eta_0} A(0, t)} \end{aligned} \tag{A.1}$$

- Face  $z = 1$ . We have  $\hat{\mathbf{n}} = \hat{\mathbf{z}}$ .

$$\begin{aligned} & \left(\hat{\mathbf{z}} \times \frac{1}{\mu_0} \nabla \times \mathbf{E}^{\text{inc}}(1, t)\right) + \frac{1}{\eta_0} \left(\hat{\mathbf{z}} \times \hat{\mathbf{z}} \times \frac{\partial \mathbf{E}^{\text{inc}}(1, t)}{\partial t}\right) = \mathbf{W}(1, t) \\ & \left(\underbrace{(\hat{\mathbf{z}} \times \hat{\mathbf{y}})}_{-\hat{\mathbf{x}}} \frac{E_0}{\eta_0} A(1, t)\right) + \frac{1}{\eta_0} \left(\underbrace{(\hat{\mathbf{z}} \times \hat{\mathbf{z}} \times -\hat{\mathbf{x}})}_{\hat{\mathbf{x}}} E_0 A(1, t)\right) = \mathbf{W}(1, t) \\ & \boxed{\mathbf{W}(1, t)} = \boxed{0} \end{aligned} \tag{A.2}$$

- Face  $y = 0$ . We have  $\hat{\mathbf{n}} = -\hat{\mathbf{y}}$ .

$$\begin{aligned} & \left(-\hat{\mathbf{y}} \times \frac{1}{\mu_0} \nabla \times \mathbf{E}^{\text{inc}}(z, t)\right) + \frac{1}{\eta_0} \left(-\hat{\mathbf{y}} \times -\hat{\mathbf{y}} \times \frac{\partial \mathbf{E}^{\text{inc}}(z, t)}{\partial t}\right) = \mathbf{W}(z, t) \\ & \left(\underbrace{(-\hat{\mathbf{y}} \times \hat{\mathbf{x}})}_0 \frac{E_0}{\eta_0} A(z, t)\right) + \frac{1}{\eta_0} \left(\underbrace{(-\hat{\mathbf{y}} \times -\hat{\mathbf{y}} \times -\hat{\mathbf{x}})}_{\hat{\mathbf{x}}} E_0 A(z, t)\right) = \mathbf{W}(z, t) \\ & \boxed{\mathbf{W}(z, t)} = \boxed{\frac{E_0 \hat{\mathbf{x}}}{\eta_0} A(z, t)} \end{aligned} \tag{A.3}$$

- Face  $y = 1$ . We have  $\hat{\mathbf{n}} = \hat{\mathbf{y}}$ .

$$\begin{aligned} & \left(\hat{\mathbf{y}} \times \frac{1}{\mu_0} \nabla \times \mathbf{E}^{\text{inc}}(z, t)\right) + \frac{1}{\eta_0} \left(\hat{\mathbf{y}} \times \hat{\mathbf{y}} \times \frac{\partial \mathbf{E}^{\text{inc}}(z, t)}{\partial t}\right) = \mathbf{W}(z, t) \\ & \left(\underbrace{(\hat{\mathbf{y}} \times \hat{\mathbf{x}})}_0 \frac{E_0}{\eta_0} A(z, t)\right) + \frac{1}{\eta_0} \left(\underbrace{(\hat{\mathbf{y}} \times \hat{\mathbf{y}} \times -\hat{\mathbf{x}})}_{\hat{\mathbf{x}}} E_0 A(z, t)\right) = \mathbf{W}(z, t) \\ & \boxed{\mathbf{W}(z, t)} = \boxed{\frac{E_0 \hat{\mathbf{x}}}{\eta_0} A(z, t)} \end{aligned} \tag{A.4}$$

- Face  $x = 0$ . We have  $\hat{\mathbf{n}} = -\hat{\mathbf{x}}$ .

$$\begin{aligned} & \left(-\hat{\mathbf{x}} \times \frac{1}{\mu_0} \nabla \times \mathbf{E}^{\text{inc}}(z, t)\right) + \frac{1}{\eta_0} \left(-\hat{\mathbf{x}} \times -\hat{\mathbf{x}} \times \frac{\partial \mathbf{E}^{\text{inc}}(z, t)}{\partial t}\right) = \mathbf{W}(z, t) \\ & \left(\underbrace{(-\hat{\mathbf{x}} \times \hat{\mathbf{y}})}_{-\hat{\mathbf{z}}} \frac{E_0}{\eta_0} A(z, t)\right) + \frac{1}{\eta_0} \left(\underbrace{(-\hat{\mathbf{x}} \times -\hat{\mathbf{x}} \times -\hat{\mathbf{z}})}_0 E_0 A(z, t)\right) = \mathbf{W}(z, t) \\ & \boxed{\mathbf{W}(z, t)} = \boxed{-\frac{E_0 \hat{\mathbf{z}}}{\eta_0} A(z, t)} \end{aligned} \tag{A.5}$$

- Face  $x = 1$ . We have  $\hat{\mathbf{n}} = \hat{\mathbf{x}}$ .

$$\begin{aligned} & \left(\hat{\mathbf{x}} \times \frac{1}{\mu_0} \nabla \times \mathbf{E}^{\text{inc}}(z, t)\right) + \frac{1}{\eta_0} \left(\hat{\mathbf{x}} \times \hat{\mathbf{x}} \times \frac{\partial \mathbf{E}^{\text{inc}}(z, t)}{\partial t}\right) = \mathbf{W}(z, t) \\ & \left(\underbrace{(\hat{\mathbf{x}} \times \hat{\mathbf{y}})}_{\hat{\mathbf{z}}} \frac{E_0}{\eta_0} A(z, t)\right) + \frac{1}{\eta_0} \left(\underbrace{(\hat{\mathbf{x}} \times \hat{\mathbf{x}} \times -\hat{\mathbf{z}})}_0 E_0 A(z, t)\right) = \mathbf{W}(z, t) \\ & \boxed{\mathbf{W}(z, t)} = \boxed{\frac{E_0 \hat{\mathbf{z}}}{\eta_0} A(z, t)} \end{aligned} \tag{A.6}$$

### Appendix B. Material constants and SI units

There was a redefinition of SI units in 2019 [24]. Specifically, the definition of the ampere underwent a major revision and, as a consequence, it affected to the definitions of vacuum permeability  $\epsilon_0$ , vacuum permittivity  $\mu_0$ , and impedance of free space  $\eta_0$ . In the following, we define these constants accordingly to what was their definition before and after 2019, respectively. It will be shown that the numerical values when expressed in SI units of the vacuum permeability  $\epsilon_0$ , vacuum permittivity  $\mu_0$ , and impedance of free space  $\eta_0$ , which were exact before the redefinition (section Appendix B.1), are subject to experimental error after the redefinition (section Appendix B.2).

From the numerical point of view, we follow definitions of section Appendix B.1 as (B.3) will be satisfied with arbitrary precision (the one that will be used when executing the code depending on hardware & software platform). The reason is that equality (B.3) is a mathematical consequence of Maxwell's Equations, i.e., is implicit to the mathematical model we will be solving numerically. Note that the definitions of the constants in section Appendix B.2 contain uncertainty and (B.3) would be satisfied only up to a given uncertainty level in that case. Analogous comments hold for (B.5).

### B.1. Before 2019 SI redefinition

For vacuum medium we define the following material constants.

$$c_0 = 299\,792\,458 \text{ m s}^{-1} \quad (\text{see note 1 below}) \quad (\text{B.1})$$

$$\mu_0 = 4\pi 0.0000001 \quad (\text{B.2})$$

Thus, as

$$c_0^2 = \frac{1}{\mu_0 \epsilon_0} (\text{m}^2 \text{s}^{-2}) \quad (\text{B.3})$$

the constant  $\epsilon_0$  has a fixed value that can be obtained (computed) as

$$\epsilon_0 = \frac{1}{c_0^2 \mu_0} (\text{F m}^{-1}) \quad (\text{B.4})$$

analogously with the free space impedance  $\eta_0$

$$\eta_0 = \sqrt{\frac{\mu_0}{\epsilon_0}} = c_0 \mu_0 (\Omega) \quad (\text{B.5})$$

Other constant that is also fixed is the product  $\sqrt{\mu_0 \epsilon_0}$  and then, we can obtain (compute) the value of the wavenumber  $k$  for a given frequency  $k$  as

$$k_0 = \omega \sqrt{\mu_0 \epsilon_0} = \frac{\omega}{c_0} (\text{m}^{-1}) \quad (\text{B.6})$$

NOTE 1: Since 1983, the metre has been defined in the International System of Units (SI) as the distance light travels in vacuum in  $1/299\,792\,458$  of a second. This definition fixes the speed of light in vacuum at exactly the value shown above.

### B.2. After 2019 SI redefinition

The definition of the ampere underwent a major revision. Details about the 2019 SI redefinition can be seen in [24]

A consequence of the revised definition is that the ampere no longer depends on the definitions of the kilogram and the metre; it does, however, still depend on the definition of the second. In addition, the numerical values when expressed in SI units of the vacuum permeability  $\epsilon_0$ , vacuum permittivity  $\mu_0$ , and impedance of free space  $\eta_0$ , which were exact before the redefinition (previous section Appendix B.1), are subject to experimental error after the redefinition.

The constants, together with its uncertainty, can be consulted at [25]. Here we simply collect the values of some constants for convenience.

$$\mu_0 = 1.256\,637\,062\,12 \times 10^{-6} \text{ N A}^{-2} \quad (\text{B.7})$$

$$\epsilon_0 = 8.854\,187\,812\,8 \times 10^{-12} \text{ F m}^{-1} \quad (\text{B.8})$$

$$\eta_0 = 376.730\,313\,668 \Omega \quad (\text{B.9})$$

## References

- [1] B. Alpert, L. Greengard, T. Hagstrom, Nonreflecting boundary conditions for the time-dependent wave equation, *J. Comput. Phys.* 180 (1) (2002) 270–296.
- [2] B. Engquist, A. Majda, Absorbing boundary conditions for the numerical simulation of waves, *Math. Comput.* 31 (1977) 629.
- [3] A. Bayliss, E. Turkel, Radiation boundary conditions for wave-like equations, *Commun. Pure Appl. Math.* 23 (1980) 707.
- [4] M. Grote, J. Keller, Nonreflecting boundary conditions for time dependent scattering, *J. Comput. Phys.* 127 (1996) 52.
- [5] I.L. Sofronov, Conditions for complete transparency on the sphere for the three-dimensional wave equation, *Russ. Acad. Sci. Dokl. Math.* 46 (1993) 397.
- [6] L. Ting, M. Miksis, Exact boundary conditions for scattering problems, *J. Acoust. Soc. Am.* 80 (1986) 1825.
- [7] P. Behnoudfar, V.M. Calo, M. Łoś, P. Maczuga, M. Paszyński, A variational splitting of high-order linear multistep methods for heat transfer and advection–diffusion parabolic problems, *J. Comput. Sci.* 63 (2022) 101807.
- [8] M. Hochbruck, T. Jahnke, R. Schnaubelt, Convergence of an ADI splitting for Maxwell's equations, *Numer. Math.* 129 (2015) 535–561.
- [9] G. Liping, Stability and super convergence analysis of ADI-FDTD for the 2D Maxwell equations in a lossy medium, *Acta Math. Sci.* 32 (6) (2012) 2341–2368.
- [10] J.A. Cottrell, T.J.R. Hughes, Y. Bazilevs, *Isogeometric Analysis: Towards Unification of Computer Aided Design and Finite Element Analysis*, John Wiley and Sons, 2009.
- [11] M. Łoś, M. Woźniak, M. Paszyński, A. Lenharth, M. Amber-Hassaan, K. Pingali IGA-ADS, Isogeometric analysis FEM using ADS solver, *Comput. Phys. Commun.* 217 (2017) 99–116.
- [12] V. Jatala, R. Dathathri, G. Gill, L. Hoang, V.K. Nandivada, K. Pingali, A study of graph analytics for massive datasets on distributed GPUs, in: *International Parallel and Distributed Processing Symposium (IPDPS)*, 2020.
- [13] <https://iss.odan.utexas.edu/?p=projects/galois> (last access: 14 Feb 2023).
- [14] L. Gao, V. Calo, Fast isogeometric solvers for explicit dynamics, *Comput. Methods Appl. Mech. Eng.* 274 (2014) 19–41.
- [15] L. Gao, V. Calo, Preconditioners based on the alternating-direction-implicit algorithm for the 2d steady-state diffusion equation with orthotropic heterogeneous coefficients, *J. Comput. Appl. Math.* 273 (2015) 274–295.
- [16] M. Łoś, M. Paszyński, A. Klusek, W. Dzwiniel, Application of fast isogeometric 12 projection solver for tumor growth simulations, *Comput. Methods Appl. Mech. Eng.* 316 (2017) 1257–1269.
- [17] M. Łoś, M. Woźniak, M. Paszyński, L. Dalcin, V. Calo, Dynamics with matrices possessing Kronecker product structure, *Proc. Comput. Sci.* 51 (2015) 286–295.
- [18] P. Behnoudfar, G. Loli, A. Reali, G. Sangalli, V.M. Calo, Explicit high-order generalized- $\alpha$  methods for isogeometric analysis of structural dynamics, *Comput. Methods Appl. Mech. Eng.* 389 (2022) 114344.
- [19] P. Behnoudfar, Q. Deng, V.M. Calo, Split generalized- method: a linear-cost solver for multi-dimensional second-order hyperbolic systems, *Comput. Methods Appl. Mech. Eng.* 376 (2021) 113656.
- [20] D.W. Peaceman, H.H. Rachford Jr., The numerical solution of parabolic and elliptic differential equations, *J. Soc. Ind. Appl. Math.* 3 (1955) 28–41.
- [21] J. Douglas, H. Rachford, On the numerical solution of heat conduction problems in two and three space variables, *Trans. Am. Math. Soc.* 82 (1956) 421–439.
- [22] J.M. Jin, *The Finite Element Method in Electromagnetics*, 3rd ed., John Wiley & Sons, Inc., 2014.
- [23] J.E. Page de la Vega, C. Camacho Penalosa, *Ondas Planas*, Departamento de Publicaciones. ETSI de Telecomunicacion. UPM, 1983.
- [24] 2019 redefinition of the SI base units — Wikipedia, the free encyclopedia, [https://en.wikipedia.org/wiki/2019\\_redefinition\\_of\\_the\\_SI\\_base\\_units](https://en.wikipedia.org/wiki/2019_redefinition_of_the_SI_base_units), (Accessed 11 November 2021), redefinition of the SI base units, online.
- [25] 2018 CODATA recommended values —the NIST reference on constants, units and uncertainty, <https://physics.nist.gov/cuu/Constants/index.html>, (Accessed 11 November 2021), online.
- [26] C.A. Balanis, *Advanced Engineering Electromagnetics*, John Wiley & Sons, Inc., 1989.
- [27] G. Mur, Absorbing boundary conditions for the finite-difference approximation of the time-domain electromagnetic-field equations, *IEEE Trans. Electromagn. Compat.* 23 (4) (1981) 377–382.